CANCER

HSF2 drives breast cancer progression by acting as a stage-specific switch between proliferation and invasion

Jenny C. Pessa[1,2], Oona Paavolainen[2,3,4], Hendrik S. E. Hästbacka[1,2], Mikael C. Puustinen[1,2], Alejandro J. Da Silva[1,2], Sandra Pihlström[1,2], Silvia Gramolelli[1,2,5], Pia Boström[6], Pauliina Hartiala[7,8], Emilia Peuhu[2,3,4]*, Jenny Joutsen[1,2,9], Lea Sistonen[1,2]*

Breast cancer is hallmarked by phenotypic transitions enabling abnormal cell proliferation and invasion. The stress-protective transcription factor heat shock factor 2 (HSF2) is associated with cancer, but its function in breast carcinogenesis remains poorly understood. Analysis of human breast tumor samples and mouse in vivo xenografts uncovered that HSF2 expression and activity undergo dynamic changes as a function of tumor progression. HSF2 expression, nuclear localization, and coexpression with the proliferation marker Ki67 are increased in ductal carcinoma in situ (DCIS), suggesting that HSF2 designates hyperplastic cells underlying tumor expansion. In mouse xenografts, HSF2 localization switches from nuclear to cytoplasmic upon DCIS-to-invasive transition. Using cell-based models, we identify canonical transforming growth factor–β (TGF-β) signaling as the molecular mechanism regulating HSF2. TGF-β–mediated down-regulation of HSF2 allowed acquisition of an invasive cell phenotype, which was counteracted by ectopic HSF2. Together, we propose that HSF2 acts as a stage-specific switch between proliferation and invasion in breast cancer.

INTRODUCTION

Breast cancer is a heterogeneous disease that follows a complex progression path where each stage is defined by unique cellular behaviors and dynamic molecular events. The most common preinvasive state of breast cancer, ductal carcinoma in situ (DCIS), is characterized by abnormal proliferation of epithelial cells within the breast ducts that are confined from the stroma by myoepithelial cells and an intact basement membrane (*1*). Although DCIS has a good prognosis, it is also considered as the nonobligate precursor of invasive ductal carcinoma (IDC). Yet, the drivers of the invasive transition remain poorly characterized, obscuring the reliable identification of high-risk lesions (*1*, *2*). In IDC, neoplastic epithelial cells have breached through the basement membrane and evaded the ductal confinement into the surrounding stromal tissue (*1*–*3*). The transition from DCIS to IDC is initiated by a subset of transformed cells that unlock the restricted capacity of phenotypic plasticity. The cell plasticity program epithelial-mesenchymal transition (EMT) plays a crucial role during invasive transition, facilitating the transition of epithelial cells into a more motile mesenchymal phenotype (*4*). The gradual changes in cellular characteristics during EMT involve the loss of cell-cell adhesions, disruption of the apicobasal polarity, and the gain of mesenchymal markers, which allow cancer cells to detach from the primary tumor and invade to adjacent tissues (*4*). The early stages of breast cancer invasion, observed as an infiltrative component in DCIS, can continue to grow into the stroma and may lead to metastasis. Throughout the different stages of breast cancer progression, dysregulated cell proliferation, driven by genetic alterations and disrupted signaling pathways, fuels tumor expansion. In addition, cancer cell properties that are antitumorigenic early on can promote cancer progression at later stages (*5*). Thus, understanding the interplay between key processes, such as cell proliferation, EMT, and invasion, is fundamental for elucidating the mechanisms driving breast cancer progression.

Many signals in the microenvironment, including cytokines and components of the extracellular matrix (ECM), can trigger EMT. Transforming growth factor–β (TGF-β) has emerged as a pivotal EMT-inducing cytokine, encompassing widespread functions, which guide development, immune modulation, cell fate decisions, and stem cell functions (*4*, *6*). Because of its multifaceted roles, disturbances to the TGF-β pathway are strongly associated with human diseases, including cancer (*7*). Under physiological conditions, TGF-β acts as a tumor suppressor by inhibiting the cell cycle and cell proliferation through regulation of cyclin-dependent kinase (CDK) activity and by inducing cell differentiation programs and apoptosis (*8*, *9*). However, mutations in various components of the TGF-β signaling pathway impair its growth inhibitory function, leading to uncontrolled proliferation of both cancer cells and stromal cells. During cancer progression, TGF-β signaling promotes ECM remodeling and cell migration through EMT induction, which enables cancer cell invasion and metastasis (*7*). In breast cancer, the aberrant activation of EMT orchestrated by TGF-β provides a mechanism underlying the acquisition of aggressive phenotypes and tumor dissemination. Activation of TGF-β signaling in breast myoepithelial cells has been implicated in promoting the invasive progression of DCIS to IDC (*3*). The signaling effects of TGF-β are mediated through transmembrane serine/threonine kinase receptors type I and type II, which can activate either a canonical signaling pathway, consisting of SMAD family proteins, or a noncanonical pathway, composed of other

[1]Faculty of Science and Engineering, Cell Biology, Åbo Akademi University, Turku, Finland. [2]Turku Bioscience Centre, University of Turku and Åbo Akademi University, Turku, Finland. [3]Institute of Biomedicine, University of Turku, Turku, Finland. [4]Western Finnish Cancer Center (FICAN West), University of Turku and Turku University Hospital, Turku, Finland. [5]InFLAMES Research Flagship Center, University of Turku and Åbo Akademi University, Turku, Finland. [6]University of Turku and Turku University Hospital, Turku, Finland. [7]Department of Plastic and General Surgery, Turku University Hospital, Turku, Finland. [8]Medicity Research Laboratories and InFLAMES Research Flagship Center, University of Turku, Turku, Finland. [9]Department of Pathology, Lapland Central Hospital, Rovaniemi, Finland.
*Corresponding author. Email: lea.sistonen@abo.fi (L.S.); emilia.peuhu@utu.fi (E.P.)

intermediators (*6*). Irrespective of the activated pathway, the cellular response to TGF-β is transmitted by specific downstream transcription factors and gene expression programs.

Heat shock factors (HSFs) are the main transcriptional regulators of the evolutionarily conserved heat shock response (*10*–*12*). Among the mammalian HSFs, HSF1 is the master stress-responsive transcription factor that can act either independently or synergistically with HSF2 (*13*). In addition to their fundamental roles in cell stress, HSFs are involved in multiple physiological and pathological processes, ranging from cell cycle regulation and differentiation to neurodevelopmental diseases and cancer (*14*–*16*). Specifically, HSF1 is exploited during tumorigenesis to induce proliferation, survival, immune escape, and metastasis through cancer-specific transcriptional programs (*17*–*20*). In breast cancer, HSF1 plays a pivotal role in disease progression by facilitating cell survival through up-regulation of molecular chaperones, cell invasion, metabolic reprogramming, inhibition of antitumor immune activity, and induction of a cancer stem cell–like state (*17*, *19*–*23*). Elevated HSF1 expression and nuclear localization also correlate with metastatic potential and reduced overall survival in patients with breast cancer (*17*, *23*, *24*). In contrast to HSF1, the role of HSF2 in tumorigenesis is poorly understood. We have previously identified HSF2 as a tumor suppressor in prostate cancer, where a decrease in HSF2 expression correlates with EMT-associated cell invasion (*25*). Other carcinoma models have revealed that HSF2 can either promote or suppress cancer cell growth (*14*), but our knowledge of its function in breast cancer is limited and the signaling pathways regulating HSF2 expression and its activity during malignant transformation remain to be uncovered. Because previous research has either used cell line models or focused on mRNA expression in advanced breast cancer (*19*, *26*), the role of HSF2 in the initial tumor stages, including DCIS and its early transition to IDC, is not known.

In this study, we analyzed human breast tumor samples and samples of a progressive mouse xenograft model mimicking the invasive transition of human DCIS. We found that HSF2 is dynamically regulated during breast cancer progression. In particular, we found that HSF2 expression, nuclear localization, and coexpression with the proliferation marker Ki67 increased strongly in human DCIS and DCIS-like mouse xenografts, suggesting that nuclear HSF2 designates the preinvasive cells with high proliferative capacity. In contrast, no changes in the coexpression of HSF1 and Ki67 were observed, indicating that HSF2 and HSF1 play divergent functions in the early stages of breast tumorigenesis. The progression from DCIS to invasion, mimicked by the mouse xenografts, was accompanied by a marked change in the subcellular localization of HSF2, shifting from nuclear to cytoplasmic. Using in vitro cell-based models, we identified the canonical TGF-β signaling pathway as the cell-intrinsic mechanism down-regulating HSF2 during EMT activation. Decreased levels of HSF2 enabled the acquisition of an invasive cell state upon TGF-β stimulation. These invasive cell properties were counteracted by ectopic HSF2 expression, highlighting the importance of HSF2 in preventing the cell state transition. Our data provide strong evidence that the expression and activity of HSF2 undergo profound changes as a function of tumor progression, where high levels mark a proliferative, noninvasive state, and low levels allow the shift toward invasion, identifying HSF2 as an important contributor to breast carcinogenesis. Collectively, we propose that dynamic regulation of HSF2 acts as a stage-specific switch between proliferation and invasion in breast cancer.

RESULTS

HSF2 displays intratumoral heterogeneity in human DCIS tumors

HSF1 has been established as a critical factor in breast cancer progression, with its increased expression and nuclear localization contributing to metastatic potential and poor patient survival (*17*, *23*, *24*). In contrast to HSF1, the role of HSF2 in breast tumorigenesis remains unexplored. Because previous research has used cell-based models (*19*), it is not known how HSF2 contributes to human breast cancer development and progression from in situ lesions to invasive carcinoma. Prompted by this gap in knowledge, we analyzed the expression and subcellular localization pattern of HSF2 in healthy human breast tissue, preinvasive DCIS, and invasive IDC (Fig. 1A). Healthy breast tissue was obtained from patients undergoing breast reduction surgery. Fixed frozen tissue sections were stained with antibodies against HSF1 and HSF2. Keratin 8 (KRT8) was used to identify cells of epithelial origin and 4′,6-diamidino-2-phenylindole (DAPI) as a nuclear marker (Fig. 1, B and C). Recently, we reported that, in formalin-fixed paraffin-embedded (FFPE) healthy human breast tissues, HSF1 is detected both in the cytoplasm and the nucleus, whereas HSF2 is expressed predominantly in the cytoplasm (*27*). Here, we found that both HSF1 and HSF2 localize in the cytoplasm of KRT8-positive breast epithelial cells in healthy breast tissue samples (Fig. 1, B and C). As expected, the expression and nuclear localization of HSF1 were substantially increased in DCIS and IDC samples when comparing to healthy tissue (Fig. 1, D to F). HSF1 was homogeneously expressed in all studied tissues (Fig. 1D), and the most abundant nuclear expression of HSF1 was observed in the IDC samples (Fig. 1F), confirming previous results (*23*, *24*). Both the total levels and nuclear localization of HSF2 were also significantly elevated in DCIS and IDC in comparison to healthy tissue, but unlike HSF1, nuclear expression of HSF2 was abundantly increased already at the DCIS stage (Fig. 1, G to I). Outstandingly, HSF2 displayed a clearly distinct expression pattern in the DCIS tumors, forming areas of enriched nuclear HSF2 in a subset of breast ducts [Fig. 1G, region of interest 1 (ROI1) versus ROI2]. The localized enrichment in HSF2 was in stark contrast to the homogeneous expression pattern of HSF1 (Fig. 1, D to G), emphasizing the difference between HSF1 and HSF2 expression patterns in DCIS. These data demonstrate that HSF2 expression increases in breast cancer and that the subcellular localization of HSF2 converts from cytoplasmic in healthy cells to nuclear in the preinvasive cells. Because nuclear localization is considered as a proxy for HSF activation (*11*, *13*), our results also suggest that there is a substantial shift in the activity of HSF2 during early breast tumorigenesis.

Subcellular localization of HSF2 switches from nuclear to cytoplasmic during mouse xenograft progression

Because of the intriguing subcellular expression pattern of HSF2 in human DCIS, we next investigated its expression in breast tumorigenesis using a mouse xenograft model. Considering that HSF2 has previously been connected to dynamic cell processes and phenotypic plasticity, including differentiation, development, and EMT (*25*, *28*, *29*), we wanted to use a model that is able to mimic the progressive changes in DCIS to IDC transition, which are difficult to capture in patient samples. The MCF10-DCIS.com (hereafter DCIS.com) xenograft model consistently recapitulates human high-grade DCIS without forming excessive intraductal hyperplasia, which frequently occur in genetically engineered mouse models (*5*, *30*–*33*). Like human DCIS, the early stages of the xenografted tumors are

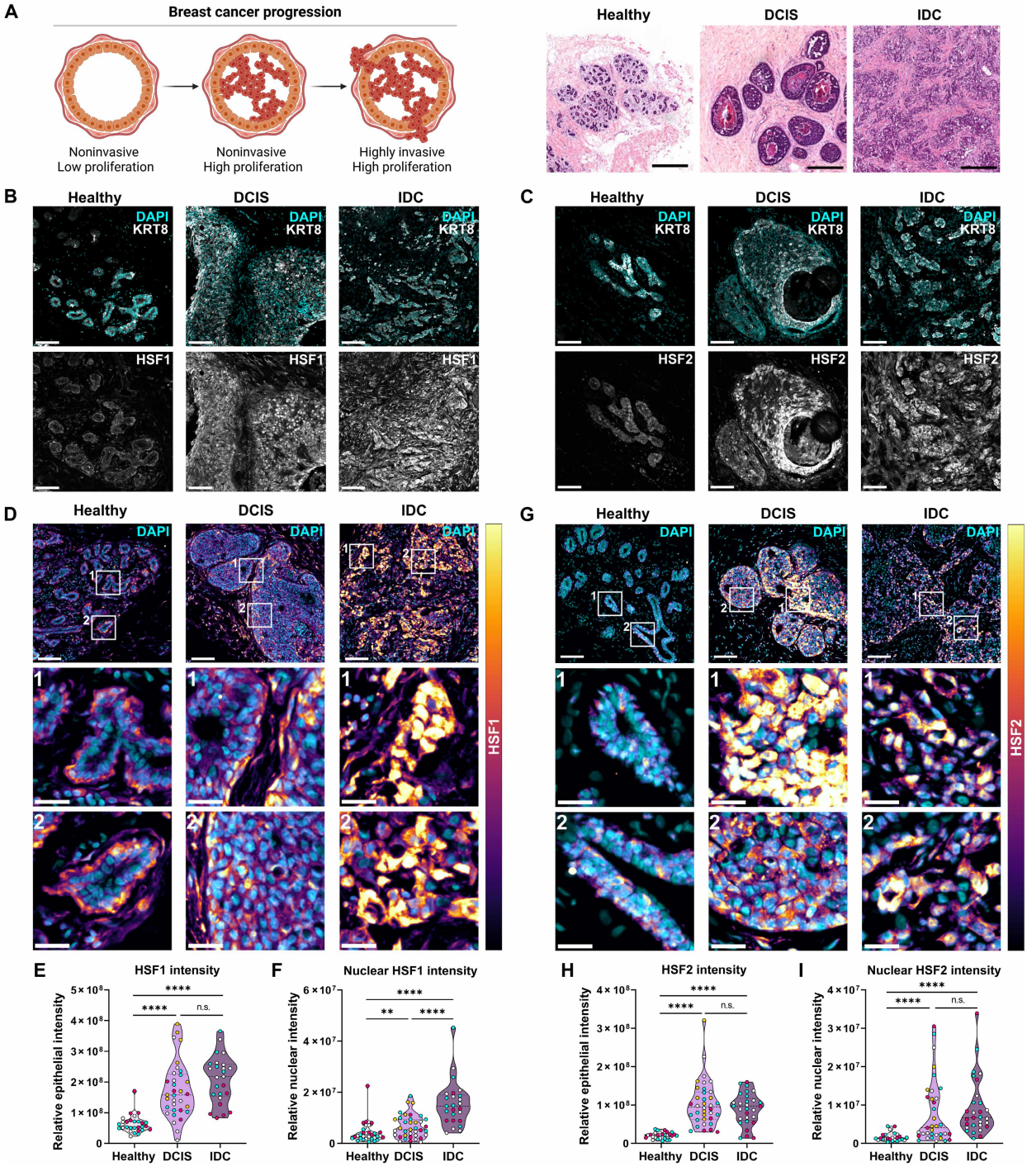

Fig. 1. HSF2 displays intratumoral heterogeneity in human DCIS tumors. (**A**) Schematic illustration of breast cancer progression and H&E staining of healthy breast, DCIS, and invasive ductal carcinoma (IDC). Scale bars, 200 μm. Left panel created in BioRender. Sistonen, L. (2025) https://BioRender.com/x4fqnd1. (**B**) Representative images from tissues immunolabeled for KRT8 and DAPI or HSF1. $n = 3$ to 4 patients. Scale bars, 100 μm. (**C**) Representative images from indicated tissues immunolabeled for KRT8 and DAPI or HSF2. $n = 3$ to 4 patients. Scale bars, 100 μm. (**D**) Representative images from tissues immunolabeled for HSF1 and DAPI. HSF1 is visualized with an intensity-coded look-up table. $n = 3$ to 4 patients. Scale bars, 100 μm (main) and 25 μm (ROIs). (**E**) Relative epithelial intensity of HSF1 presented as violin plots, $^{****}P < 0.0001$; n.s., not significant. $n = 3$ to 4 patients. For each patient, 6 to 10 fields of view (FOVs) were quantified. Data point colors indicate the patient origin. (**F**) Relative nuclear intensity of HSF1 presented as violin plots, $^{**}P < 0.01$; $^{****}P < 0.0001$. $n = 3$ to 4 patients. For each patient, 6 to 10 FOVs were quantified. Data point colors indicate the patient origin. (**G**) Representative images from tissues immunolabeled for HSF2 and DAPI. HSF2 is visualized with an intensity-coded look-up table. $n = 3$ to 4 patients. Scale bars, 100 μm (main) and 25 μm (ROIs). (**H**) Relative epithelial intensity of HSF2 presented as violin plots, $^{****}P < 0.0001$; n.s., not significant. $n = 3$ to 4 patients. For each patient, 6 to 10 FOVs were quantified. Data point colors indicate the patient origin. (**I**) Relative nuclear intensity of HSF2 presented as violin plots, $^{****}P < 0.0001$; n.s., not significant. $n = 3$ to 4 patients. For each patient, 6 to 10 FOVs were quantified. Data point colors indicate the patient origin.

surrounded by a basement membrane and a layer of cells positive for myoepithelial markers (*5*, *31*). DCIS.com cells were injected subcutaneously into nonobese diabetic–severe combined immunodeficient (NOD-SCID) female mice, and the animals were euthanized at indicated time points (Fig. 2A). The dissected xenograft tumors were processed for fixation and immunolabeling with HSF2. The histology of xenograft tumors resected after 10 and 25 days resembled human DCIS and invasive tumor morphology, respectively (Fig. 2B). Similarly to our data obtained from human tumor tissues (Fig. 1), the total intratumoral intensity of HSF2 was not altered between DCIS-like and invasive xenografts (Fig. 2, C and D). Instead, we found that HSF2 was expressed at high levels in the nucleus of cells in DCIS-like tumors (Fig. 2, C and E). Upon invasive progression, a notable change in the subcellular localization of HSF2 was detected, demonstrating that HSF2 switches from being predominantly nuclear in the DCIS-like tumors to almost exclusively cytoplasmic in the invasive xenografts (Fig. 2C). In addition, nuclear HSF2 exhibited similar intratumoral heterogeneity as in patient DCIS samples (Figs. 1G and 2C). Our findings provide evidence that the subcellular localization of HSF2 undergoes profound changes as a function of tumor progression, suggesting a stage-specific role for HSF2 as a mediator of cell phenotypic changes during the DCIS-to-invasive transition.

HSF2 is down-regulated in response to TGF-β–induced EMT

The cell plasticity program EMT characterizes the transition from localized to invasive cancer (*4*). We have previously shown that down-regulation of HSF2 coincides with EMT and invasiveness in prostate cancer cells (*25*). However, the molecular mechanism underpinning the loss of HSF2 during EMT, and whether it is a common regulatory step in the phenotypic transition of other carcinoma cells, is not known. Together with our findings from human tissue samples (Fig. 1) and mouse xenografts (Fig. 2), demonstrating a dynamic expression pattern for HSF2 in breast cancer progression, we asked whether HSF2 contributes to the cell phenotypic shift through EMT. We addressed this question by inducing EMT in human breast epithelial cells. Transformed (HS578T and MDA-MB-231) and nontransformed (MCF10A) human breast epithelial cells were treated with an EMT-inducing supplement containing recombinant human transforming growth factor–β 1 (TGF-β_1, hereafter TGF-β), Wnt family member 5A, antibodies against human E-cadherin, secreted frizzled-related protein 1, and Dickkopf-related protein 1. A 24-hour treatment with the EMT supplement significantly reduced the levels of HSF2 protein in all studied cell lines (fig. S1A). By using a selective small molecule inhibitor of the TGF-β type I receptor, SB431542, we demonstrated that the reduction of HSF2 is a specific downstream event of the TGF-β type I receptor activation (fig. S1A).

Upon EMT, tumor cells lose their epithelial characteristics and acquire a mesenchymal phenotype. To investigate whether the ability of TGF-β to down-regulate HSF2 is a specific property of the epithelial phenotype, we treated both breast epithelial cells and mesenchymal human dermal fibroblasts (HDFs) with TGF-β (Fig. 3A). The efficacy of TGF-β treatment was first confirmed in HS578T cells by analyzing the phosphorylation status of SMAD2 (*34*) and the protein levels of the EMT marker Snail (*35*). A 20-min treatment already caused a prominent phosphorylation of SMAD2 (fig. S1B), and Snail was substantially up-regulated in response to a 24-hour treatment (fig. S1C), showing that the TGF-β treatment was sufficient to activate the signaling pathway. Intriguingly, HSF2 was not affected by TGF-β in HDFs, but a robust down-regulation was observed in human breast epithelial cells (Fig. 3A and fig. S2A), indicating that the TGF-β–induced down-regulation of HSF2 is unique for cells of epithelial origin. In sharp contrast to HSF2, the protein levels of HSF1 remained unchanged in all examined cell lines (Fig. 3A and fig. S2A). By treating MDA-MB-231 HSF1 knockout cells (HSF1-KO) (*19*) with TGF-β, we confirmed that HSF2 is down-regulated in response to the treatment irrespective of HSF1 (fig. S2B). Thus, we identified the canonical TGF-β signaling pathway as the cell-intrinsic mechanism down-regulating HSF2 in breast cancer cells during EMT.

Forced HSF2 expression disrupts TGF-β–regulated gene programs

Down-regulation of HSF2 upon TGF-β treatment suggests that HSF2 is one of the downstream effector transcription factors of the TGF-β signaling pathway. We next examined the TGF-β–induced gene programs that depend on HSF2 down-regulation and whether forced expression of HSF2 would disrupt this gene expression signature. HS578T cells were transiently transfected with plasmids encoding either green fluorescent protein (GFP) ($Mock^T$) or exogenous HSF2 ($HSF2oe^T$). The transient expression of HSF2 was sufficient to override the down-regulating effect of TGF-β on HSF2 without affecting HSF1 protein levels (Fig. 3B and fig. S2C). Overexpression of HSF2 did not interfere with activation of the TGF-β signaling pathway, as indicated by induced SMAD2 phosphorylation and unchanged levels of total SMAD2/3 in response to TGF-β treatment (fig. S2, D and E). The global gene expression profiles of $Mock^T$ and $HSF2oe^T$ cells were analyzed by RNA sequencing (RNA-seq) in the presence and absence of TGF-β stimulation. In $Mock^T$ cells, the treatment resulted in up-regulation of well-known TGF-β target genes, *IL11*, *SNAI1*, *WNT1*, and *CDH2* (N-cadherin) (fig. S3A), confirming the functionality of our treatment. Next, we addressed the specific role of HSF2 in the TGF-β signaling pathway by identifying the TGF-β–responsive genes that are dependent on the loss of HSF2. In the presence of ectopically expressed HSF2, a set of 131 genes displayed impaired ability to respond to TGF-β (Fig. 3C and fig. S3B). These genes were divided into four different categories on the basis of their expression pattern (Fig. 3D and data S1): group I, genes up-regulated by both TGF-β and exogenous HSF2; group II, genes up-regulated by TGF-β but not in the presence of exogenous HSF2; group III, genes down-regulated by both TGF-β and exogenous HSF2; and group IV, genes down-regulated by TGF-β but not in the presence of exogenous HSF2.

The assigned groups were subjected to gene ontology (GO) term analysis, which showed that group I and II genes were associated with vascular functions and ECM remodeling (Fig. 3E, top), and groups III and IV were associated with DNA replication and cell cycle regulation (Fig. 3E, bottom). As examples of group I and II genes, *ADAMTS10*, *ACTA2*, *ITGA1*, *COL8A2*, and *PDGFRB* were markedly increased in control cells treated with TGF-β, and their up-regulation was abolished in cells expressing exogenous HSF2 (Fig. 3F, top). ADAM metallopeptidase with thrombospondin type 1 motif 10 (ADAMTS10) is a regulator of ECM composition (*36*, *37*), and actin alpha 2 (ACTA2) affects the cellular ability to form cell-cell and cell-matrix adhesions (*38*, *39*). Extensive remodeling of the ECM and cell adhesion contacts are hallmarks of EMT-induced invasion and required for cancer progression. In addition, the transmembrane receptor integrin subunit alpha 1 (ITGA1) is strongly connected to TGF-β–induced EMT and metastasis (*40*). As examples of group

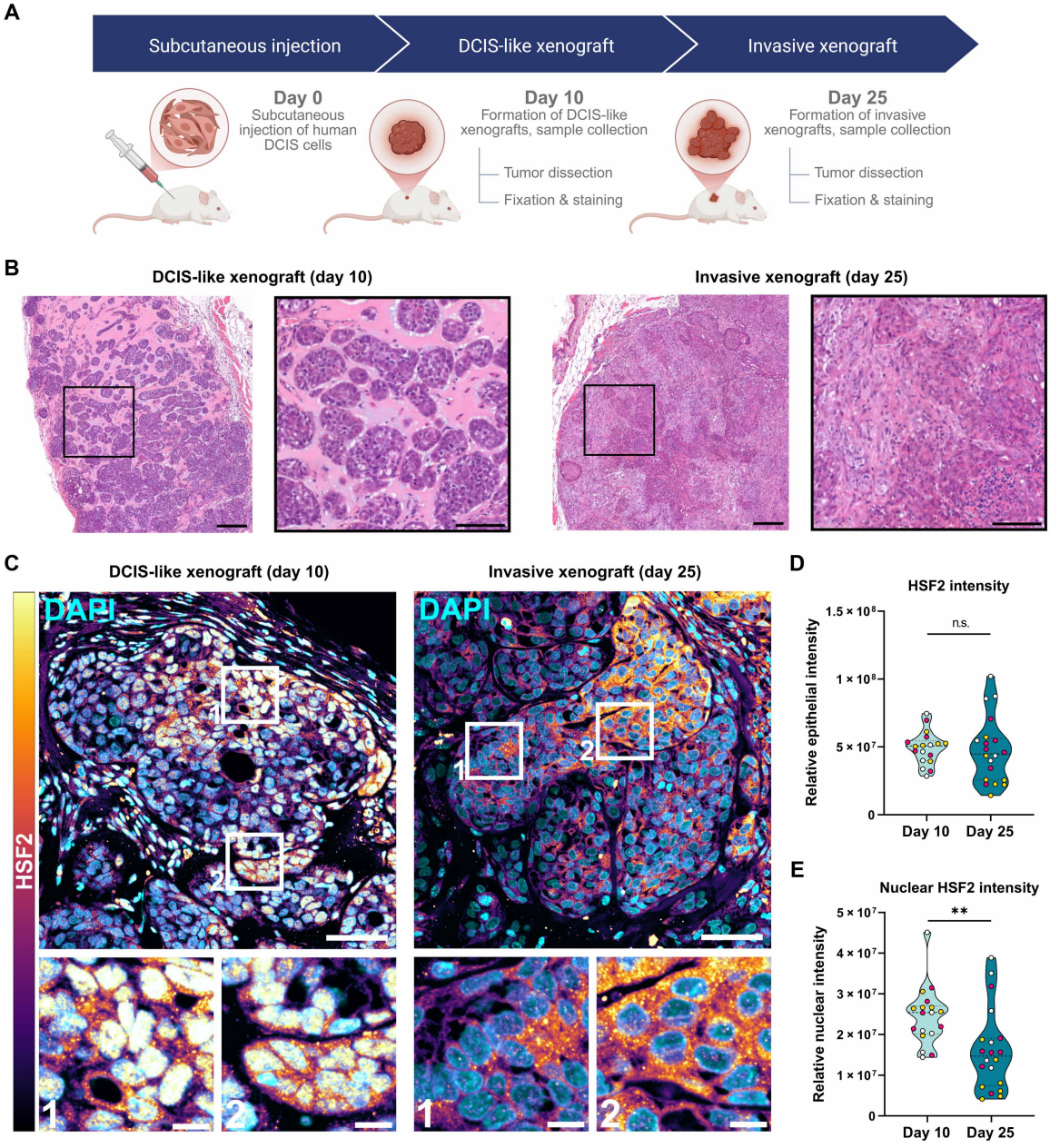

Fig. 2. HSF2 subcellular localization changes from nuclear to cytoplasmic during mouse xenograft progression. (**A**) Schematic illustration of tumor progression stages in the MCF10-DCIS.com mouse xenograft model. DCIS-like tumors and invasive tumors form within 10 and 25 days, respectively, after subcutaneous inoculation of human DCIS.com cells into NOD-SCID mice. Created in BioRender. Sistonen, L. (2025) https://BioRender.com/uh5gztl. (**B**) Representative H&E staining of tissue sections from DCIS-like (day 10) and invasive (day 25) mouse xenografts. Scale bars, 200 μm (main) and 100 μm (inset). (**C**) Representative immunofluorescence images from DCIS-like and invasive mouse xenografts tissue sections immunolabeled for HSF2 and DAPI. HSF2 labeling intensity is visualized with an intensity-coded look-up table (high values: yellow). $n = 3$ mice. Scale bars, 50 μm (main) and 10 μm (inset). (**D**) Relative intensity of HSF2 labeling in the epithelial area (KRT8$^+$) of mouse xenograft tumors dissected at indicated time points. Results are presented as violin plots, n.s., not significant. $n = 3$ mice. For each mouse, five to seven FOVs were quantified. Colors of data points (white, yellow, and red) indicate the mouse origin. (**E**) Relative intensity of HSF2 labeling in the nuclei (DAPI$^+$) of the epithelial area (KRT8$^+$) of mouse xenograft tumors dissected at indicated time points. Results are presented as violin plots, $^{**}P < 0.01$. $n = 3$ mice. For each mouse, five to seven FOVs were quantified. Colors of data points (white, yellow, and red) indicate the mouse origin.

III and IV genes, *HELLS*, *DNA2*, *RAD51AP1*, *CDC45*, and *GINS1* were decreased in TGF-β–treated control cells, and their downregulation was inhibited by overexpression of HSF2 (Fig. 3F, bottom). Cell division cycle 45 (CDC45) and proliferating nuclear antigen (PCNA) proteins are critical for DNA replication initiation and progression, respectively (*41*, *42*). It has previously been shown that TGF-β inhibits the loading of CDC45 and PCNA onto chromatin, thereby preventing the activation of minichromosome maintenance complex (MCM), a DNA helicase vital for DNA replication (*43*). The TGF-β–mediated inhibition disturbs the assembly of both prereplication complexes (Pre-RCs) and preinitiation complexes (Pre-IRs), which leads to cell cycle arrest at G_1-S (*44*). These results demonstrate

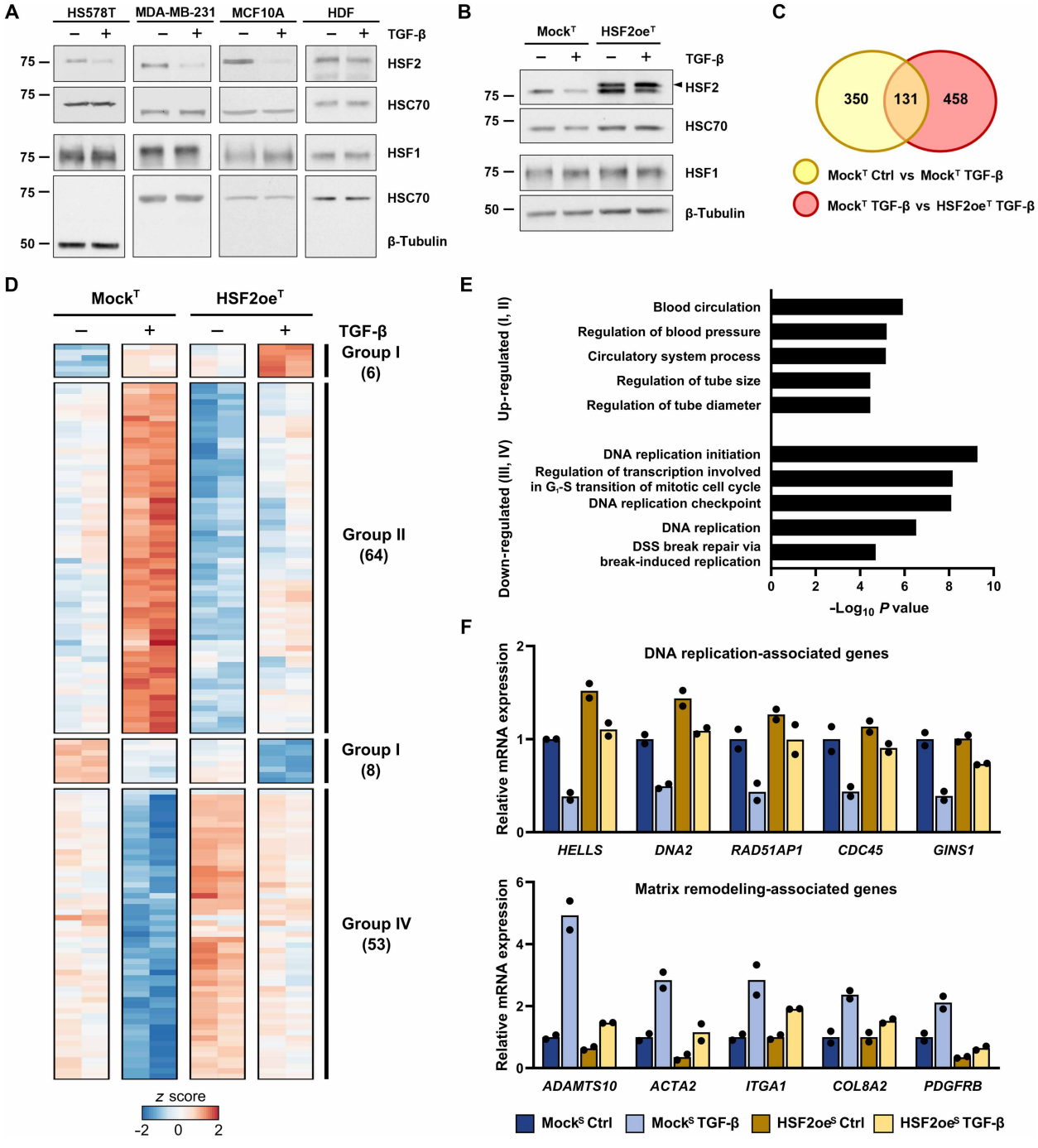

Fig. 3. Ectopic HSF2 bypasses down-regulation by TGF-β and disrupts TGF-β–regulated gene programs. (**A**) Immunoblot analysis of HSF2 and HSF1 protein levels in HS578T, MDA-MB-231, and MCF10A cells as well as HDFs treated with TGF-β_1 (10 ng/ml) or assay medium for 24 hours. HSC70 and β-tubulin were used as a loading control. (**B**) Immunoblot analysis of HSF2 and HSF1 protein levels in Mock^T and HSF2oe^T HS578T cells treated with TGF-β_1 (10 ng/ml) or assay medium for 24 hours. Arrowhead (◄) denotes exogenous HSF2. HSC70 was used as a loading control. (**C**) Venn diagram of differentially expressed (DE) genes. The overlapping region represents a subset of 131 TGF-β target genes, whose expression was impaired by HSF2 overexpression. (**D**) Heatmap of the 131 DE genes identified in (C) and categorized into four groups: group I, genes up-regulated by both TGF-β and exogenous HSF2; group II, genes up-regulated by TGF-β but impaired response in the presence of exogenous HSF2; group III, genes down-regulated by both TGF-β and exogenous HSF2; and group IV, genes down-regulated by TGF-β and impaired response in the presence of exogenous HSF2. The *z* score was calculated on the basis of the $\log_2$CPM values for each gene. The double columns for each condition represent the two biological replicates from the RNA-seq. (**E**) GO term analysis of the 131 DE genes identified in (C) and categorized in (D). The five most significant biological processes are shown. The analysis was performed with topGO. (**F**) Relative mRNA expression of a subset of the 131 DE genes associated with matrix remodeling and DNA replication. The relative difference in CPM between conditions was normalized to the CPM of the Mock^T Ctrl for each gene. The data represent two biological replicates, which are indicated by individual data points. CPM, counts per million.

that ectopic HSF2 interferes with the expression of genes characteristic for TGF-β–induced EMT.

Exogenous HSF2 counteracts TGF-β–induced cell migration and stabilizes cell-cell adhesions

TGF-β is well known for its multifaceted roles in the regulation of ECM composition and cell adhesion (*6*, *7*). Thus, we expanded our gene expression analyses to include more components of the ECM and cell adhesion receptors, which revealed that a comprehensive selection of the genes was unable to respond to TGF-β in the presence of exogenous HSF2 (Fig. 4A). To investigate whether the observed changes in mRNA expression were also detected on protein level, we performed immunoblotting of selected targets. Because of slower changes in the protein levels, we extended the TGF-β treatment from 24 to 72 hours. As transiently expressed HSF2 declined already at 72 hours (fig. S4A), stable HS578T cell lines expressing either GFP (Mock^S) or HSF2 (HSF2oe^S) were generated (fig. S4B). Mock^S cells maintained their responsiveness to TGF-β stimulation and HSF2oe^S cells displayed sustained expression of HSF2 upon a 72-hour TGF-β treatment (fig. S4C). Two ECM proteins, i.e., collagen type III alpha chain 1 (COL3A1) and matrix metalloproteinase 2 (MMP2), were markedly increased in Mock^S cells treated with TGF-β for 72 hours, but only low expression was observed in HSF2oe^S cells (Fig. 4B and fig. S5A). Both proteins are direct TGF-β targets, and their elevated expression promotes tumorigenesis via enhanced ECM remodeling in a variety of cancers (*45*, *46*). Similarly, the integrin subunit alpha 1 (ITGA1) protein was markedly up-regulated in Mock^S cells but remained unchanged in HSF2oe^S cells (Fig. 4B and fig. S5A). In contrast, the amount of cell-cell adhesion receptor E-cadherin (CDH1), a classical epithelial state marker (*4*), was induced in HSF2oe^S cells in comparison to Mock^S cells (Fig. 4B and fig. S5A). Moreover, immunofluorescence staining highlighted the diminished expression of COL3A1 and integrin subunit beta 1 (ITGB1) in HSF2oe^S cells (fig. S5, B to D), suggesting that HSF2 overexpression interferes with cell-matrix adhesion and ECM secretion.

Because of the robust changes in gene expression and protein levels of ECM modifiers and cell-matrix adhesion receptors, we explored the functional impact of HSF2 on cell migration and invasion. First, in vitro vasculogenic mimicry assay was used to study the ability of Mock^S and HSF2oe^S cells to modulate the ECM and reorganize into tube-like structures in three dimensions, in the presence and absence of TGF-β (fig. S6A). The Mock^S cells formed complex and interconnected networks, and treatment with TGF-β further augmented network formation as measured by the number of master segments (fig. S6, B and C). In stark contrast, HSF2oe^S cells displayed impaired organization into tube-like networks despite the treatment as measured by several parameters (fig. S6, B to D). Specifically, the difference in number of segments, total meshes area, and total branching length between the Mock^S and HSF2oe^S cells (fig. S6B) established that HSF2 attenuates the cellular ability to modify the ECM.

Using a wound healing assay, we investigated whether the down-regulation of HSF2 in response to TGF-β is sufficient to induce cell migration. MDA-MB-231 cells, with high migratory capacity (*47*), were transfected with either HSF2oe^T or Mock^T plasmids, and the expression of exogenous HSF2 was verified by immunoblotting (Fig. 4C and fig. S7A). TGF-β was added 3 hours before initiation of the assay to ensure that the cells had activated the TGF-β signaling pathway. Analysis of the relative wound closure revealed that the TGF-β treatment stimulated migration of Mock^T cells, whereas HSF2oe^T cells displayed a substantial reduction in cell motility (Fig. 4, D and E). These results indicate that TGF-β–mediated down-regulation of HSF2 facilitates increased migration of breast cancer cells.

Deterioration of cell-cell adhesion contacts is a hallmark of TGF-β–induced EMT (*4*). We have previously shown that HSF2 localizes at cell-cell adhesion sites in several human tissues (*27*) and interacts with the focal adhesion adapter protein talin 1 (*48*). Accordingly, the loss of HSF2 leads to disrupted cell-cell adhesion (*49*, *50*). Prompted by these findings, we examined whether the TGF-β–mediated decrease in HSF2 influenced cell-cell adhesion of breast cancer cells and whether the functional consequences could be reversed by overexpression of HSF2. The capacity of MDA-MB-231 Mock^T and HSF2oe^T cells to maintain cell-cell adhesion contacts was analyzed using ultralow attachment (ULA) round-bottom plates, where a covalently bonded hydrogel surface of the wells stimulates the formation of spheroid-like structures. Transfected cells were treated with TGF-β alone or in combination with the selective TGF-β type I receptor inhibitor, SB431542, for 24 hours in ULA plates. Mock^T cells formed compact spheroid-like structures under control conditions, and the TGF-β treatment diminished this capacity (Fig. 4, F and G), which is indicative of destabilized cell-cell adhesions. Addition of SB431542 to the TGF-β–treated cells restored their potential to form spheroid-like structures (Fig. 4F). Intriguingly, HSF2oe^T cells formed compact structures even in the presence of TGF-β (Fig. 4F), which denotes preserved cell-cell adhesions. Quantification of the spheroid areas corroborated our results (Fig. 4G), demonstrating that TGF-β–mediated down-regulation of HSF2 leads to impaired cell-cell adhesion and forced expression of HSF2 counteracts the TGF-β–induced destabilization of cell-cell contacts.

HSF2 overrides the TGF-β–mediated inhibition of cell proliferation

Under physiological conditions and early phases of tumorigenesis, TGF-β is an important cell cycle regulator and inhibits cell growth by modulating the expression of CDKs and CDK inhibitors (*8*, *9*, *51*). Our RNA-seq analysis indicated that the major gene groups that were down-regulated by TGF-β signaling but lost their responsiveness upon HSF2 overexpression are related to cell cycle progression (Fig. 3, E and F). To gain more insight into how HSF2 affects the TGF-β–mediated regulation of the cell cycle, we expanded our analysis to include more genes important for DNA replication and cell proliferation, such as members of the MCM complex, the GINS gene family, and cell cycle–associated kinases. Intriguingly, the expression of the examined genes was decreased by TGF-β, whereas overexpression of HSF2 dysregulated the TGF-β–dependent transcriptional changes (Fig. 5A). These results are in line with a recently published study reporting that HSF1 and HSF2 regulate the expression of cell cycle–associated genes across multiple human cancer cell lines, including those derived from breast, prostate, lung, and colon cancer (*19*).

We next analyzed the protein levels of selected targets in Mock^S and HSF2oe^S cells that were either treated with TGF-β or left untreated for 72 hours. Origin recognition complex 1 (ORC1), a factor that promotes initiation of DNA replication by maintaining MCM helicases at the origin sequence (*52*), increased substantially in cells expressing exogenous HSF2 in comparison to Mock^S cells (Fig. 5B and fig. S7B). Similarly, minichromosome maintenance protein 2

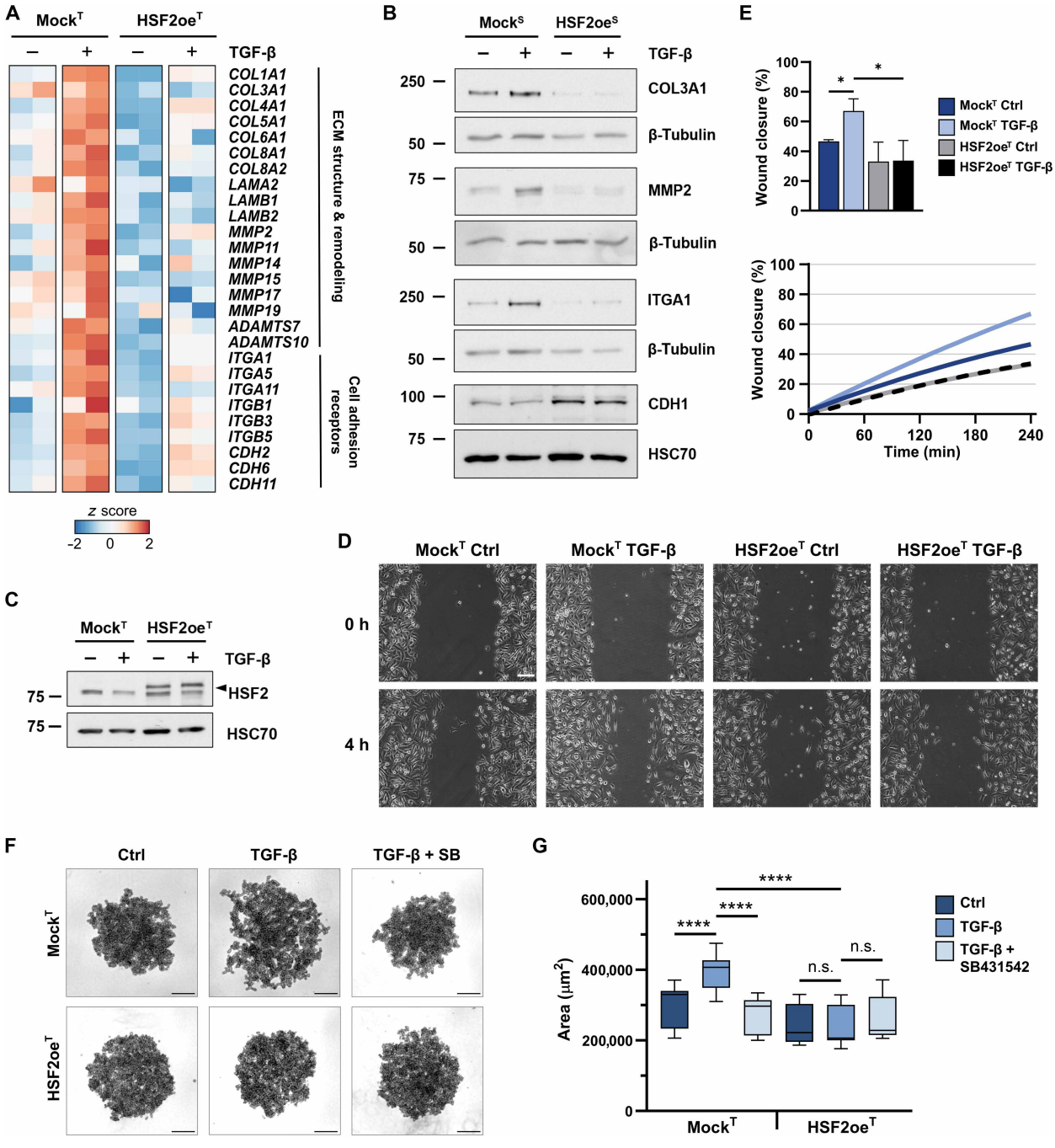

Fig. 4. HSF2 interferes with the expression of ECM and cell-matrix receptor proteins. (**A**) Heatmap illustrating expression changes of genes in Mock^T and HSF2oe^T HS578T cells treated with TGF-β_1 (10 ng/ml) or assay medium for 24 hours. The *z* score was calculated on the basis of log_2CPM values for each gene. Double columns represent two biological replicates. (**B**) Immunoblot analysis of COL3A1, MMP2, ITGA1, and CDH1 levels in Mock^S and HSF2oe^S cells treated with TGF-β_1 (10 ng/ml) or assay medium for 72 hours. β-Tubulin and HSC70 were used as loading controls. (**C**) Immunoblot analysis of HSF2 levels in Mock^T and HSF2oe^T MDA-MB-231 cells treated with TGF-β_1 (10 ng/ml) or assay medium for 24 hours. Arrowhead (◄) denotes exogenous HSF2. HSC70 was used as a loading control. (**D**) Representative images of wound closure at 0 and 4 hours (h). Mock^T and HSF2oe^T cells were treated with TGF-β_1 (10 ng/ml) or assay medium (Ctrl). The rate of wound closure was monitored with live-cell imaging using a 5-min frame interval. Scale bar, 100 μm. (**E**) Quantitative analysis of wound healing assay. The percentage of wound closure was calculated by normalizing the wound area of each time point to the initial scratch area. Results were plotted as means ± SD, $*P \leq 0.05$. The data represent three biological replicates. (**F**) Representative images of spheroid-like structure formation. Mock^T and HSF2oe^T cells were incubated in assay medium (Ctrl) or treated with TGF-β_1 alone (10 ng/ml) or in combination with 10 μM SB431542 for 24 hours. Scale bars, 200 μm. (**G**) Quantification of spheroid size. The average area between biological replicates was calculated, and the relative area for each condition was normalized to the average area of Mock^T Ctrl. Results were plotted as means ± SEM, $****P \leq 0.0001$. The data represent three biological replicates.

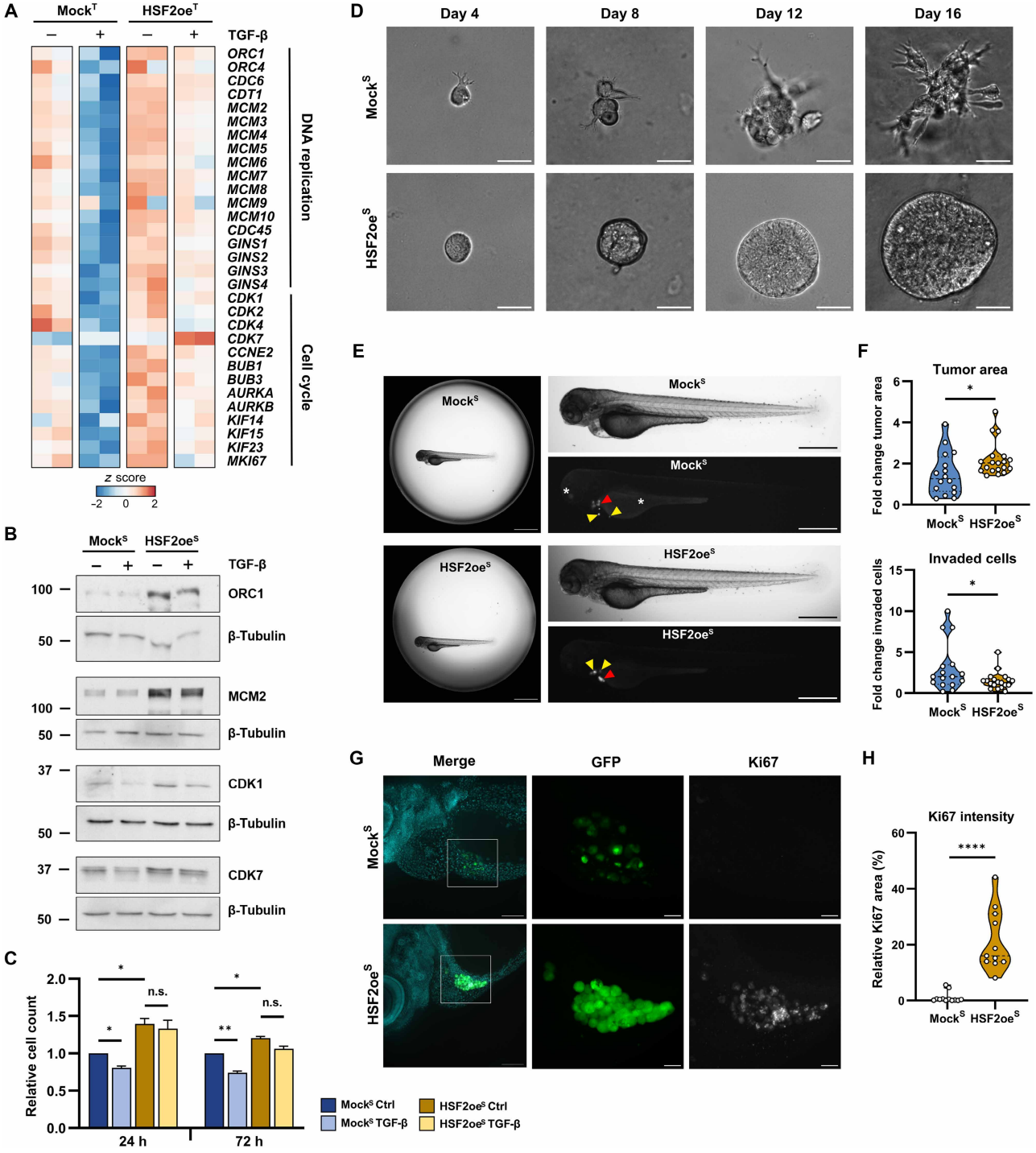

Fig. 5. HSF2 promotes proliferation in vitro and in vivo. (**A**) Heatmap illustrating expression changes of genes in Mock^T and HSF2oe^T HS578T cells treated with TGF-β_1 (10 ng/ml) or assay medium for 24 hours. The *z* score was calculated on the basis of $\log_2$CPM values for each gene. Double columns represent two biological replicates. (**B**) Immunoblot analysis of ORC1, MCM2, CDK1, and CDK7 proteins in Mock^S and HSF2oe^S cells treated with TGF-β_1 (10 ng/ml) or assay medium for 72 hours. β-Tubulin was used as a loading control. (**C**) Proliferation analysis of Mock^S and HSF2oe^S cells treated with TGF-β_1 (10 ng/ml) or assay medium (Ctrl) for 24 or 72 hours. Results are presented as means ± SEM, $^*P < 0.05$; $^{**}P < 0.01$; n.s., not significant. The data represent three biological replicates. (**D**) Representative images of Mock^S and HSF2oe^S organotypic 3D cultures. Formation of organotypic tumoroids was followed up to 16 days. Scale bars, 200 μm. The data represent three biological replicates. (**E**) Bright-field and fluorescence images of Mock^S and HSF2oe^S zebrafish xenografts. Red arrowheads indicate the primary tumor, and yellow arrowheads indicate disseminated cancer cells. Asterisk (*) denotes unspecific fluorescence. Scale bars, 1 mm (main) and 500 μm (inset). (**F**) Quantification of tumor area and invaded cells in Mock^S and HSF2oe^S xenografts. Results are presented as means ± SD, $^*P < 0.05$. For Mock^S 16 and for HSF2oe^S 19, xenografts were analyzed. (**G**) Representative images of Mock^S and HSF2oe^S zebrafish xenografts immunolabeled with DAPI (cyan) and Ki67. White square indicates areas of insets. Scale bars, 100 μm (main) and 25 μm (inset). (**H**) Relative Ki67 area in Mock^S and HSF2oe^S xenograft tumors. Results are presented as means ± SEM, $^{****}P < 0.0001$. For Mock^S 12 and for HSF2oe^S 11, xenografts were analyzed.

(MCM2), a key component of the Pre-RC involved in the initiation of eukaryotic genome replication (*53*), was elevated in HSF2oe^S cells (Fig. 5B and fig. S7B). The expression levels of CDKs 1 and 7 (CDK1 and CDK7), both well-known regulators of cell cycle progression (*54*, *55*), were also increased in HSF2oe^S cells (Fig. 5B and fig. S7B).

TGF-β signaling affects cell proliferation in normal and tumor cells, and the mode of action can vary depending on the phase in which the cell is in its life cycle or stage of tumorigenesis (*56*). To examine the effect of HSF2 on cell proliferation, Mock^S and HSF2oe^S cells were subjected to TGF-β for either 24 or 72 hours. Using the Cell Counting Kit-8 (CCK-8) assay, we quantified the differences in cell amounts that are indicative of cell proliferation. In line with previous findings demonstrating that Snail inhibits cell cycle progression (*57*), the TGF-β treatment decreased cell proliferation of Mock^S cells when compared to untreated cells (Fig. 5C). Cell proliferation was markedly higher in HSF2oe^S cells, and there was no notable change between the untreated and TGF-β–treated cells (Fig. 5C). On the basis of these results, we propose that the loss of HSF2 is a requirement for the TGF-β–mediated inhibition of cell proliferation.

To further assess the proliferation and invasion capacity of Mock^S and HSF2oe^S cells, we analyzed three-dimensional (3D) Matrigel cultures where the formation of organotypic tumoroids was followed up to 16 days. Mock^S cells started developing invasive structures already at day 4, which gradually increased toward the end point of the assay (Fig. 5D). HSF2oe^S cells failed to form invasive structures despite the rapid growth (Fig. 5D), thereby supporting our data on induced proliferation of HSF2oe^S cells (Fig. 5C). Upon activation of invasive behavior, malignant cells reduce their proliferation to enable enhanced migration (*58*). Thus, our results showed that Mock^S cells stopped proliferating to induce cell migration, whereas the ability of the rapidly proliferating HSF2oe^S cells to become invasive was inhibited.

HSF2 promotes proliferation and secondary tumor formation in in vivo zebrafish xenografts

After performing cell-based in vitro assays, we wanted to know whether the obtained results were applicable also in vivo. For this purpose, we examined the capacity of Mock^S and HSF2oe^S cells to promote tumor growth and invasiveness using the zebrafish xenografts (*59*, *60*). Cells were nanoinjected into the pericardial cavity of 2-day-old zebrafish embryos, and the xenografts were imaged at 1 day postinjection (1 dpi) and 4 dpi (Fig. 5E). In comparison to Mock^S, HSF2-overexpressing cells displayed larger tumor area and impaired invasion capacity (Fig. 5F), reinforcing the anti-invasive effect of HSF2 in breast cancer cells. To more closely examine the proliferation rate of Mock^S and HSF2oe^S cells, we analyzed the expression of proliferation marker Ki67 in the formed xenograft tumors by immunofluorescence. The cells were again nanoinjected into the pericardial cavity of zebrafish embryos, and after 24 hours, the animals were fixed and stained with DAPI and Ki67 (Fig. 5G). Immunofluorescence analysis revealed that the HSF2oe^S xenografts displayed clearly more abundant Ki67 expression than the Mock^S xenografts (Fig. 5G). Furthermore, analysis of the relative Ki67 area within the tumors demonstrated that a significantly larger proportion of the HSF2oe^S cells were Ki67 positive (Fig. 5H), corroborating that HSF2 drives cell proliferation and tumor expansion in vivo. Together, our results from cell-based in vitro and in vivo assays demonstrate that whereas TGF-β–mediated down-regulation of HSF2 occurs concomitantly with EMT, elevated levels of HSF2 are critical for supporting malignant cell proliferation and tumor growth.

Nuclear coexpression of HSF2 and Ki67 increases in DCIS-like mouse xenografts and human DCIS tumors

We have identified that HSF2 displays a highly heterogeneous expression pattern in human DCIS tumors (Fig. 1) and that exogenous HSF2 drives the expression of cell cycle–associated genes (Fig. 3) and accelerates proliferation in cell-based in vitro models and in vivo zebrafish xenografts (Fig. 5). On the basis of these results, we hypothesized that nuclear HSF2 contributes to a hyperplastic cell phenotype and tumor growth in DCIS. To explore this hypothesis, we immunolabeled proliferating tumor cells with Ki67 and examined the proportion of proliferative cells that showed nuclear HSF2. In the progressive breast cancer xenograft model, the coexpression of HSF2 and Ki67 was significantly increased in the DCIS-like tumors (Fig. 6, A and B), showing that HSF2 could contribute to the preinvasive tumor expansion. Although coexpression of HSF2 and Ki67 varied among the samples of invasive xenografts, the areas displaying prominent coexpression resembled DCIS-like tumor morphology (Fig. 6B).

Last, we analyzed the expression pattern of HSF2 and Ki67 in the proliferative cells of healthy breast, DCIS, and IDC human tumor samples (Fig. 6C). Our results revealed that the coexpression of HSF2 and Ki67 in the nucleus increased significantly in the DCIS tumors and remained elevated in the invasive IDC tumors (Fig. 6, C and D). Combined with the results demonstrating markedly increased nuclear HSF2 expression in both DCIS and IDC samples (Fig. 1, G and I), our data suggest that nuclear HSF2 is a specific feature of actively proliferating tumor cells in breast cancer. These results demonstrate that HSF2 designates the preinvasive cells with high proliferative capacity and suggest that the areas with enriched HSF2 may function as the central sites of tumor expansion. Notably, no alterations were observed in the coexpression pattern of nuclear HSF1 and Ki67 across the examined tissue samples (Fig. 6, E and F). Collectively, we conclude that, unlike HSF1, which mainly supports malignancy in advanced breast cancer, HSF2 acts as a stage-specific switch between the proliferative and invasive phenotypes at the initial steps of breast cancer progression.

DISCUSSION

The functional role of HSF2 in breast cancer and the signaling pathways regulating its activity have remained largely unknown. Here, by using a selection of in vitro and in vivo assays combined with analysis of patient samples, we show that dynamic regulation of HSF2 contributes to distinct stages of breast cancer progression (Fig. 7). Our results uncover that elevated levels of nuclear HSF2 designate the epithelial cells with high proliferative capacity in human breast tumors. In mouse xenografts, the early transition from DCIS to invasion is accompanied by a switch in the subcellular localization of HSF2 from nuclear to cytoplasmic, suggesting a change in its activity. Furthermore, using cell-based models, we identify the canonical TGF-β signaling pathway as the cell-intrinsic mechanism underpinning HSF2 down-regulation in breast cancer cells during EMT. The TGF-β–mediated decrease in HSF2 allowed acquisition of an invasive phenotype, which was counteracted by ectopic expression of HSF2. On the basis of our results, we present a model in Fig. 7, where high levels and nuclear accumulation of HSF2 drive

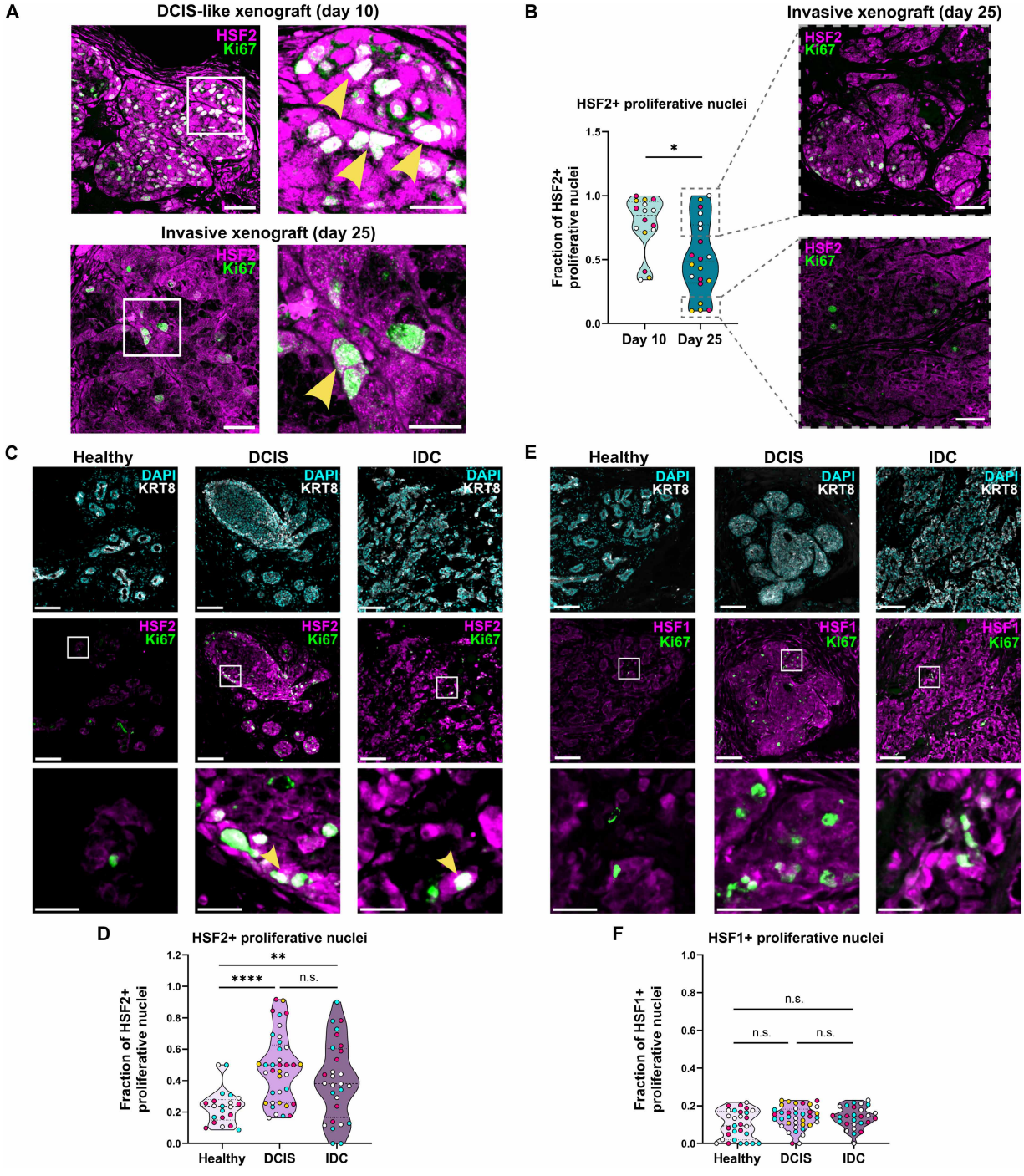

Fig. 6. Nuclear localization of HSF2 increases in the proliferating cells of DCIS-like mouse xenografts and human DCIS tumors. (**A**) Representative images from DCIS-like and invasive MCF10-DCIS.com mouse xenografts immunolabeled for HSF2 and Ki67. Nuclei positive for both HSF2 and Ki67 are visualized as white (indicated by yellow arrowheads). White square indicates areas of insets. $n = 3$ mice. Scale bars, 50 μm (main) and 25 μm (inset). (**B**) Quantification of HSF2-positive ($HSF2^+$) nuclei among proliferating cells ($Ki67^+$). Results are presented as violin plots, $^*P < 0.05$. $n = 3$ mice. For each mouse, four to seven FOVs were quantified. Data point colors (white, yellow, and red) indicate the mouse origin. Images from day 25 xenografts demonstrate the heterogeneity of DCIS-like and invasive tumor areas and the association of nuclear HSF2 with $Ki67^+$ proliferative and DCIS-like areas. (**C**) Representative images from human tissues immunolabeled for KRT8 and DAPI or HSF2 and Ki67. Nuclei positive for both Ki67 and HSF2 are visualized as white (indicated by yellow arrowheads). $n = 3$ to 4 patients. Scale bars, 100 μm (main) and 25 μm (ROIs). (**D**) Quantification of HSF2-positive (HSF2+) proliferative cells within the epithelium. Results are presented as violin plots, $^{**}P < 0.01$; $^{****}P < 0.0001$; n.s., not significant. $n = 3$ to 4 patients. For each patient, 6 to 10 FOVs were quantified. Data point colors (white, yellow, cyan, and red) indicate the patient origin. (**E**) Representative images of human tissues immunolabeled for KRT8 and DAPI or HSF1 and Ki67. $n = 3$ to 4 patients. Scale bars, 100 μm (main) and 25 μm (ROIs). (**F**) Quantification of HSF1-positive (HSF1+) proliferative cells within the epithelium. Results are presented as violin plots. n.s., not significant. $n = 3$ to 4 patients. For each patient, 6 to 10 FOVs were quantified. Data point colors indicate the patient origin.

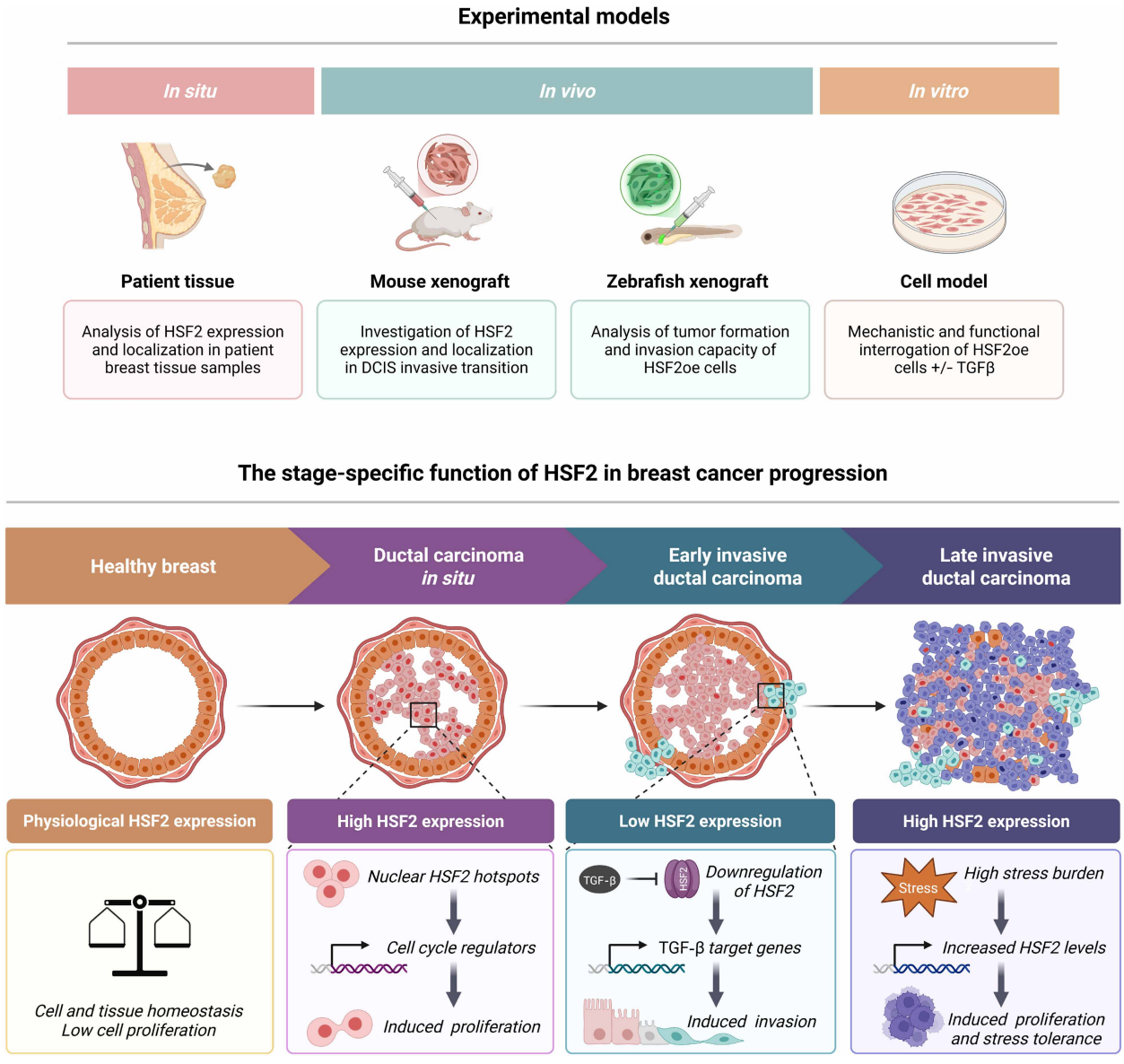

Fig. 7. Stage-specific function of HSF2 in breast cancer progression. Summary of experimental models used to analyze the function of HSF2 in breast cancer progression (**Top**). A schematic model of the stage-specific function of HSF2 during different states of breast cancer progression (**Bottom**). In the normal breast epithelium, physiological HSF2 expression contributes to the maintenance of cell and tissue homeostasis. In the preinvasive stage of breast cancer, DCIS, increased expression, and nuclear accumulation of HSF2 activate the transcription of genes regulating the cell cycle, leading to induced proliferation of ductal epithelial cells. At the early stage of invasive ductal carcinoma, protumorigenic TGF-β signaling leads to a transient down-regulation of HSF2 to enable expression of TGF-β target genes and activation of the EMT program in a subset of transformed cells (turquoise). Subsequently, cells undergoing EMT acquire induced migratory abilities and invade through the basement membrane, forming microinvasions around the breast ducts. At the late stage of invasive ductal carcinoma, high stress burden in the tumor microenvironment leads to elevated levels of HSF2 expression and nuclear localization to promote proliferation, stress tolerance, and cancer cell survival. Created in BioRender. Sistonen, L. (2025) https://BioRender.com/1wrn1ie.

cell proliferation in the preinvasive DCIS. In contrast, a temporal down-regulation of HSF2 through protumorigenic TGF-β signaling activates EMT, thereby allowing cancer cell invasion. At the invasive cancer stage, elevated HSF2 expression supports stress tolerance and sustains proliferation of cancer cells (Fig. 7). Our findings provide clear evidence that the expression and activity of HSF2 undergo profound changes as a function of tumor progression, identifying HSF2 as a critical contributor of breast cancer progression. Collectively, we propose that dynamic regulation of HSF2 acts as a stage-specific switch in breast cancer, where high levels of HSF2 drive cell proliferation and preinvasive tumor expansion, and low levels promote the phenotypic changes required for invasive transitioning and metastatic potential.

Previous studies have recognized HSF1 as a nononcogenic driver in cancer, steering tumor-supportive transcriptional programs in both cancer cells and the adjacent cancer-associated fibroblasts (CAFs) (*17*–*20*, *61*). Moreover, because of its prominent disease-supporting role, several inhibitors targeting HSF1 have been developed (*62*–*64*).

To date, no HSF2-specific pharmacological inhibitors are available. HSF2 has been reported as a critical cofactor of HSF1 in driving a transcriptional program to support the malignant state of several human cancer cell lines, including breast, prostate, colon, and lung cancer cells (*19*). In this study, however, we could not observe any changes in HSF1 expression upon TGF-β treatment, and HSF1 was not directly involved in the TGF-β–mediated regulation of HSF2 levels. The robust down-regulation of HSF2 was evident already within 24 hours of TGF-β stimulation, mimicking the primary steps of the invasive transition. These findings support the divergent functions of HSF1 and HSF2 explicitly at the initial phases of malignant transformation. TGF-β is one of the main cytokines mediating the interplay between tumor cells and CAFs (*65*), and it is secreted by CAFs in an HSF1-dependent manner (*18*). In colon cancer, HSF1 is up-regulated in CAFs where it regulates the expression and secretion of TGF-β and stromal cell–derived factor 1, another important cytokine supporting tumor growth (*18*). In addition, HSF1 contributes to stromal heterogeneity by modulating the ratio of immune-regulatory clusterin-positive CAFs in pancreatic ductal adenocarcinoma with germline mutations in the BRCA gene (*61*). In the MCF10-DCIS.com xenograft model, TGF-β is initially expressed by the cancer cells during early tumor formation and its expression is gradually increased in stromal cells during cancer progression (*66*), further supporting the role of TGF-β as a proinvasive signaling cue. Considering the previous reports and the results obtained in this study, it is tempting to speculate that the intercellular signaling between CAFs and cancer cells occurs through cross-talk mediated by HSFs. Accordingly, HSF1 in CAFs stimulates TGF-β secretion allowing adjacent cancer cells to initiate prometastatic cell processes due to TGF-β–induced down-regulation of HSF2. This would describe an unprecedented non–cell-autonomous regulation of HSFs, exemplifying that their impact on cancer progression is more multifaceted than previously anticipated. Thereby, future studies should focus on the mechanisms by which CAF-secreted TGF-β affects HSF2 in malignant cells and elucidate the possible cross-talk of HSF1 and HSF2 in tumorigenesis.

The initiation and early invasive growth of epithelial carcinomas is characterized by the activation of EMT. During EMT, cells lose their epithelial-specific cell-cell junctions and acquire a more motile mesenchymal phenotype with the ability to modify the local microenvironment (*4*). TGF-β is one of the key cytokines promoting EMT, and it acts through a selection of transcription factors, which repress the expression of E-cadherin, control the reorganization of cytoskeletal proteins, and enable the production of ECM components (*4*, *6*). Our data using the selective TGF-β type I receptor inhibitor (SB431542) (fig. S1A) showed that the down-regulation of HSF2 is prevented during EMT stimulation in the presence of the inhibitor (fig. S1A), suggesting that the down-regulation of HSF2 is mediated through the canonical TGF-β signaling pathway. However, we cannot exclude the possibility that other noncanonical EMT signaling pathways, such as MAPK, PI3K/AKT, and JAK/STAT (*4*), might be involved in regulating HSF2 levels and activity. Here, we observed that HSF2 overrides this regulatory pathway as HSF2-overexpressing cells displayed substantially elevated protein levels of E-cadherin and were able to stabilize cell-cell adhesions even in the presence of TGF-β. In addition, forced expression of HSF2 blocked the TGF-β–mediated up-regulation of several key invasion-associated matrix proteins and diminished the ability of in vitro vasculogenic mimicry. The Hannon laboratory recently showed that the transcription factor FOXC2 promotes vasculogenic mimicry in several solid tumors (*67*), whereas we identified HSF2 as a suppressor of vasculogenic mimicry in breast cancer cells. Furthermore, by investigating cell migration in both in vitro 3D cell cultures and in vivo zebrafish xenografts, we identified that the presence of HSF2 markedly impairs cellular invasiveness. These results indicate that HSF2 prevents epithelial cells from acquiring a mesenchymal phenotype. We have previously reported that the lack of HSF2 leads to down-regulation of cadherin-mediated cell-cell adhesions in osteosarcoma cells (*49*). More recently, the importance of HSF2 in neuroepithelial integrity was highlighted in organoids modeling the Rubinstein-Taybi neurodevelopmental disorder, where destabilization of HSF2 caused dysregulation of N-cadherin in neuronal cells (*50*). On the basis of these results, we connect high levels of HSF2 to the maintenance of an epithelial phenotype, whereas activation of EMT and the transition toward a quasimesenchymal cell state is accompanied by TGF-β–mediated down-regulation of HSF2. Because ectopic HSF2 was sufficient to maintain epithelial properties, i.e., increased levels of E-cadherin, reduced migration, and stabilization of cell-cell adhesions even in the presence of TGF-β, we propose that loss of HSF2 is required for the acquisition of an invasive phenotype during TGF-β–induced EMT. Cells that undergo EMT-linked phenotypic switching are typically considered as cells eventually entering the invasion-metastasis cascade. Once metastasized, cells have the possibility to revert to a more epithelial phenotype by using the reverse process of EMT, i.e., mesenchymal-epithelial transition (*68*). Hence, it is plausible that HSF2 expression is restored in the established secondary tumor to promote growth.

The dynamic regulation of HSF2 expression has been described in multiple developmental and differentiation-related processes, including cell cycle, spermatogenesis, and embryonal development (*12*, *16*). An example is mouse embryogenesis, where HSF2 levels fluctuate markedly (*28*, *29*). Our findings in cell-based models, mouse xenografts, and human tissue samples portray an equally dynamic expression and activation pattern of HSF2 during breast cancer progression (Fig. 7). We demonstrated that HSF2 is up-regulated, and its nuclear localization increased in DCIS and IDC. Curiously, HSF2 showed a distinct expression pattern with a strong nuclear accumulation in DCIS, where it was coexpressed with the proliferation marker Ki67. Recently, mice xenografted with MDA-MB-231 cells lacking HSF2 displayed reduced tumor size and increased survival in comparison to control xenografts (*19*). Moreover, chromatin immunoprecipitation sequencing results from the same study revealed that HSF2 binds to several cell cycle– and proliferation-associated genes. Although we did not detect an overlap with the targets in our RNA-seq data, this further supports the tumor growth–promoting function of HSF2 in breast cancer.

Ki67 is commonly used as a prognostic marker for invasive breast cancer, and its high levels are associated with an elevated risk of DCIS recurrence (*2*, *69*, *70*). Yet, the drivers of the invasive transition from DCIS to IDC are poorly characterized and current biomarkers are unable to reliably distinguish the high-risk lesions (*2*). On the basis of our results, we speculate that the areas with enriched nuclear HSF2 are hubs for accelerated cell proliferation that might function as the underlying sites for preinvasive tumor expansion. How these HSF2-high areas relate to the invasive transition could be described by two, not mutually exclusive hypotheses. First, it is possible that the sites with enriched nuclear HSF2 are also more prone to invasive transition, potentially due to additional factors, including alterations in

the tumor microenvironment or proinvasive signals such as aberrant TGF-β signaling. Accordingly, the invasive transition would be marked by a notable but transient down-regulation of HSF2 in a subset of cancer cells that undergo invasion. This hypothesis is further supported by clinical data from the Human Protein Atlas, which shows that high levels of HSF2 mRNA correlate with poor survival outcomes in patients with breast cancer (https://proteinatlas.org/ENSG00000025156-HSF2/cancer). In addition, our results demonstrate that HSF2 is coexpressed with Ki67, one of the few prognostic markers used in breast cancer diagnostics, further strengthening the idea of HSF2 as a potential biomarker. According to the second hypothesis, it is plausible that persistent nuclear HSF2 expression would restrain invasive progression, functioning as a gatekeeper for invasiveness. In this case, HSF2 could instead help define the low-risk DCIS lesions and serve as a prognostic biomarker for tumors that remain noninvasive. Ultimately, whether high nuclear HSF2 identifies DCIS tumors at high- or low-risk of invasion depends on resolving the fate of HSF2-high DCIS cells. Either outcome would provide clinically valuable information. A majority of currently used clinical biomarkers are, however, used as on-off switches, where the diagnostic readout is the expression of the protein of interest, e.g., the status of HER-2, ER, and PR (*2*). Our results strongly indicate that not only the expression level per se but also the localization pattern of a protein, such as HSF2, might be a relevant prognostic determinant. Taken that intratumoral heterogeneity poses one of the major challenges for developing efficient cancer diagnostic and therapeutic approaches, attention should be directed to interrogate local changes within a tumor. Hence, further characterization of the HSF2-rich areas in DCIS, using advanced spatial proteomics in combination with systematic DCIS patient analyses, is required to fully assess the prognostic and therapeutic potential of HSF2.

In this work, we found that HSF2 expression and activity undergo profound changes as a function of tumor progression. In comparison to healthy breast tissue, the expression, nuclear localization, and coexpression of HSF2 with Ki67 were increased already at the DCIS stage, indicating that HSF2 designates the hyperplastic cell phenotype that underlies tumor expansion. Notably, HSF2 exhibited intratumoral heterogeneity in distinct areas of DCIS tumors. The DCIS-to-invasive transition, as mimicked by mouse xenografts, was accompanied by a marked shift in HSF2 localization from nuclear in DCIS to cytoplasmic in invaded xenografts. By using human breast cancer cells, we identified the canonical TGF-β signaling pathway as the underlying molecular mechanism down-regulating HSF2 during EMT activation. The TGF-β–mediated reduction of HSF2 facilitated acquisition of an invasive cell phenotype, which could be reversed by ectopic HSF2. Together, our results reveal HSF2 as a stage-specific switch between proliferation and invasion in breast cancer.

Limitations of the study

Our study reports that HSF2 is dynamically regulated and acts as a stage-specific switch between the proliferative and invasive states during early breast carcinogenesis. By combining analyses of patient breast tissue samples with cell-based in vitro and in vivo assays, we demonstrate that HSF2 expression and localization change as a function of tumor progression. Unexpectedly, we did not observe changes in HSF1 expression upon TGF-β treatment nor did HSF1-KO affect the TGF-β–mediated down-regulation of HSF2. Although our results suggest that HSF1 might not directly regulate HSF2 in this specific context, we cannot preclude the possibility that HSF1 and HSF2 would act in a coordinated or antagonistic manner during later stages of breast cancer progression. Forthcoming studies should address the potential functional interplay between HSF1 and HSF2 during the EMT-mediated transition to invasive breast cancer. Although in vivo xenograft models provide valuable insights into tumor growth and invasion, immunocompromised mice do not fully recapitulate the complexity of the human tumor microenvironment. Nevertheless, the molecular, cellular, and histopathological changes in DCIS-like mouse xenografts resemble human high-grade DCIS, making it a suitable model to study DCIS progression to invasion. Conditional deletion or activation of HSF2 using tissue-specific Cre-loxP systems would further characterize the detailed stage-specific function of HSF2. In addition, lineage tracing would allow tracking of the progeny of HSF2-high cells to establish whether they are the source of the invasive transition. Although our results from patient samples present a strong correlation between high levels of nuclear HSF2, increased cell proliferation, and tumorigenesis, future research should analyze larger clinical cohorts to identify whether the nuclear accumulation of HSF2 specifically corresponds to certain breast cancer subtypes.

MATERIALS AND METHODS

Cell culture, treatments, and transient transfections

Cells were grown at 37°C in a humidified 5% CO_2 atmosphere. Human transformed breast epithelial MDA-MB-231 cells, human embryonic kidney (HEK) 293T cells, and HDFs were cultured in Dulbecco's modified Eagle's medium (DMEM; Sigma-Aldrich), supplemented with 10% fetal bovine serum (FBS; Serena), 2 mM L-glutamine (Biowest), and penicillin-streptomycin (100 μg/ml; Biowest). Human HS578T transformed breast epithelial cells were cultured in DMEM supplemented with 10% FBS, 2 mM L-glutamine, penicillin-streptomycin (100 μg/ml), and insulin (10 μg/ml; A11382II, Gibco). Human MCF10A and MCF10-DCIS.com breast epithelial cells were cultured in DMEM/F12 (DMEM/Nutrient Mixture F-12, Gibco) supplemented with 5% fetal horse serum (Gibco), insulin (10 μg/ml), hydrocortisone (0.5 μg/ml; Sigma-Aldrich), epidermal growth factor (20 ng/ml), cholera toxin (100 ng/ml; Sigma-Aldrich), and penicillin-streptomycin (100 μg/ml). All used cells were immortalized cell lines and routinely tested to ensure negative mycoplasma status.

For treatments, the medium was supplemented with 2% serum (referred to as assay medium). Cells were treated with assay medium supplemented with TGF-β_1 (10 ng/ml; hereafter referred to as TGF-β, 240-B-002, R&D Systems) for 24 or 72 hours (*35*). For the longer treatment, the medium was replaced after 48 hours. To induce canonical and noncanonical TGF-β signaling, cells were treated with assay medium supplemented with StemXVivo EMT Inducing Media Supplement (EMT supplement, CCM017, R&D Systems). To inhibit TGF-β signaling, cells were treated with 10 μM SB431542 (S4317, Sigma-Aldrich), a TGF-β receptor type 1 inhibitor.

All transient transfections were performed with the Neon Transfection System (MPK5000, Invitrogen) according to the manufacturer's instructions. In brief, 1.8×10^6 HS578T or 2.2×10^6 MDA-MB-231 cells were suspended in 100 μl of Buffer R containing either 25 μg of plasmid and/or 3 μM small interfering RNA. Next, HS578T and MDA-MB-231 cells were subjected to electroporation (1050 V, 20 ms, three pulses and 1350 V, 10 ms, four pulses, respectively) in the

transfection tube containing 3 ml of Buffer E2. Transfected cells were allowed to recover for 24 hours before the treatments.

Generation of stable cell lines

HEK-293T cells were cultured in a T25 flask to a confluency of 70 to 80%. The next day, cells were transfected using Lipofectamine 3000 (Thermo Fisher Scientific) in accordance with the manufacturer's instructions. Briefly, 14 μl of Lipofectamine reagent was mixed with 500 μl of Opti-MEM in a 1.5-ml microcentrifuge tube, and in a separate tube, viral vectors pLP1 (1.7 μg), pLP2 (1.1 μg), PLP/VSVg (1.7 μg), and the expression vector (1.5 μg) were mixed in 500 μl of Opti-MEM containing 12 μl of p3000 reagent. Expression vectors containing either GFP alone ($Mock^S$) or HSF2 and GFP ($HSF2oe^S$, connected with a T2A sequence) were designed and purchased from VectorBuilder. Each microcentrifuge tube was carefully mixed by pipetting and incubated for 15 min at room temperature (RT). Meanwhile, 4 ml of fresh DMEM was added to each T25 flask and following the incubation period the transfection mix was added dropwise to the cells. Thereafter, cells were incubated at 37°C with 5% CO_2 overnight. The next day, the medium was replaced in each flask. The supernatant containing the virus was collected 72 hours posttransfection and centrifuged for 10 min at 1000*g*. The pool of viral medium was filtered through a 0.45-μm pore size filter, supplemented with polybrene (8 μg/ml) and applied on HS578T cells in a 6-well plate. Next, spinoculation was performed at 450*g* for 30 min at RT. The medium was changed 48 hours posttransduction, and antibiotic selection with puromycin was started 72 hours posttransduction. Following 2 weeks of culturing, the negative lentiviral status was confirmed for each cell line using the HIV-1 p24 DuoSet ELISA rom kit (DY7360-05, R&D Systems).

Plasmid construction

The plasmid encoding exogenous HSF2 was generated by inserting a fragment containing the protein coding sequence of HSF2 and a myc-tag. In addition, a Strep-Tag II, purchased from Eurofins Genomics, was placed downstream of the myc-tag. Polymerase chain reaction was used to amplify the whole fragment containing a cytomegalovirus (CMV) promoter, HSF2-myc-StrepII, and an SV40 (polyA) tail, which was inserted into a pEGFP-N2 vector (GenBank accession no. U57608). The final construct (HSF2oe) enabled exogenous expression of both HSF2-myc-Strep II and GFP via separate CMV promoters. The pEGFP-N2 plasmid was used as Mock. All primer sequences used for plasmid constructions are listed in table S2.

Immunoblotting

Cells were washed in cold phosphate-buffered saline (PBS) (Biowest), after which they were lysed and boiled in 3x Laemmli lysis buffer (30% glycerol, 187.5 mM SDS, 3% tris-HCl, 0.015% bromophenol blue, and 3% β-mercaptoethanol), resolved on a self-cast 8% SDS–polyacrylamide gel or on 7.5% or 4 to 20% Mini-PROTEAN TGX Stain-Free Precast Gels (Bio-Rad), and transferred onto a Amersham Protran 0.45 nitrocellulose membrane (Cytiva). For detecting HSF2, the membranes were boiled in Milli-Q H_2O for 20 min and blocked with 5% milk–PBS–Tween 20. Membranes blotted with phospho-specific antibodies were blocked with 2% bovine serum albumin (BSA)–tris-buffered saline (TBS)–Tween 20. The following antibodies were used for immunoblotting with a 1:1000 dilution: anti-HSF2 (HPA031455, Sigma-Aldrich), anti-HSF1 (ADI-SPA-901, Enzo Life Sciences), anti-HSC70 (ADI-SPA-815, Enzo Life Sciences), anti-β-Tubulin (T8328, Sigma-Aldrich), anti-Snail (C15D3, Cell Signaling Technology), anti-SMAD2/3 (3102, Cell Signaling Technology), anti-pSMAD2 (138D4, Cell Signaling Technology), anti-ORC1 (7A7, BioNordika), anti-MCM2 (D7611, BioNordika), anti-ITGA1 (22146-1-AP, Proteintech), anti-COL3A1 (22734-1-AP, Proteintech), anti-MMP2 (10373-2-AP, Proteintech), anti-CDK1 (A17, ab18, Abcam), anti-CDK-7 (sc-7344, Santa Cruz Biotechnology), and anti-E-cadherin (24E10, Cell Signaling Technology). Horseradish peroxidase–conjugated secondary antibodies were purchased from Promega and GE Healthcare and used with a 1:10,000 dilution. Immunoblots were quantified with FIJI software using the gel analysis tool, and the measured values were normalized to respective loading controls. All immunoblots represent three biological replicates unless otherwise indicated.

Immunofluorescence of cultured cells

For immunofluorescence, 2×10^5 GFP^S and 4×10^5 $HSF2oe^S$ HS578T cells were seeded on MatTek plates (P35GC-1.5-14-C, MatTek Corporation) 48 hours before fixation. After 24 hours, the medium was changed to assay medium only for control samples or to assay supplemented with TGF-β (10 ng/ml) for treatments. Following a 24-hour treatment, cells were fixed with 4% paraformaldehyde (PFA) for 10 min, washed three times with PBS, permeabilized with 0.5% Triton X-100 and 3 mM EDTA in PBS for 30 min, and washed again three times with PBS. The cells were then blocked with 10% FBS in PBS for 1 hour at RT and incubated with primary antibodies overnight at 4°C. The following primary antibodies were diluted in 10% FBS-PBS: 1:200 anti-COL3A1 (22734-1-AP, Proteintech) and 1:100 anti-ITGB1 (12G10, Abcam). After primary antibody incubation, cells were washed three times with PBS and incubated with secondary antibodies for 1 hour at RT. The following secondary antibodies were diluted in 10% FBS-PBS: 1:500 Alexa Fluor 546 goat anti-rabbit (A11035, Life Technologies), 1:500 Alexa Fluor 555 donkey anti-mouse (A31570, Life Technologies), and 1:500 Alexa Fluor 633 goat anti-mouse (A21052, Invitrogen). Next, the cells were washed once with PBS, incubated with 300 nM DAPI in PBS for 5 min, washed again once with PBS, and covered with VECTASHIELD mounting medium (H-100, Vector Laboratories). Images were taken with a 3i CSU-W1 spinning disk confocal microscope using a 20x objective (Intelligent Imaging Innovations). Acquired images are shown as maximum intensity projections (MIPs). The images were analyzed with FIJI software. First, the background was subtracted from MIPs using a rolling ball radius of 50 pixels. Next, the area of COL3A1 and ITGB1 signals were segmented by manual thresholding and the intensities within these segmented areas were measured. The relative intensities of COL3A1 and ITGB1 in the cells were then calculated for each sample by dividing the obtained integrated density value with the measured area. Last, the relative intensity value for each sample was normalized to the mean of $Mock^S$ control.

RNA sequencing

HS578T cells were transiently transfected with plasmids encoding GFP ($Mock^T$) or HSF2 ($HSF2oe^T$). After a 24-hour recovery, the cells were incubated in assay medium supplemented with TGF-β (10 ng/ml) or assay medium (Ctrl) for 24 hours. Cells were collected, and RNA was purified from the samples using the AllPrep DNA/RNA/miRNA Universal Kit (80224, QIAGEN) according to the manufacturer's instructions. The amount of RNA was quantified using a NanoDrop 2000 spectrophotometer (Thermo Fisher Scientific). Before sequencing, the RNA library was prepared according to Illumina

stranded mRNA preparation guide (1000000124518). Briefly, poly-A–containing mRNA molecules were isolated using poly-T oligo magnetic beads and fragmented with divalent cations under elevated temperatures. The first-strand cDNA synthesis was performed wherein RNA fragments were copied using reverse transcriptase and random primers. In the second-strand cDNA synthesis, dUTP (deoxyuridine triphosphate) replaced dTTP (deoxythymidine triphosphate) to achieve strand specificity. Unique dual indexing adapters were ligated to each sample, and the quality and concentration of cDNA samples were analyzed with Advanced Analytical Fragment Analyzer and Bioanalyzer 2100 (Agilent) and Qubit Fluorometric Quantitation (Life Technologies). Samples were sequenced with NovaSeq 6000 S1 v1.5. All the experimental steps after the RNA extraction were conducted at the Finnish Functional Genomics Centre core facility (Turku, Finland). RNA-seq was performed from two independent sample series.

Analysis of RNA-seq data

FastQC v0.11.9 was used to confirm the quality of the raw reads, and the paired-end reads were aligned to the human genome (primary assembly GRCh38.p13, GENCODE) with STAR version 2.7.9a (*71*), using the default settings. The number of read pairs mapped to each genomic feature in release 38 of the GENCODE annotation was determined by featureCounts from subread v2.0.1 (*72*). Only read pairs with both ends aligned were counted. Differential gene expression analysis was performed using the Bioconductor R package edgeR (version 3.34.1) (*73*). Lowly expressed genes were filtered out (using filterByExpr defaults), and the samples were normalized using the trimmed mean of M-values (TMM) method. The threshold for differentially expressed genes was set to FDR (false discovery rate) < 0.05, and the gene expression data were visualized as an MA plot, produced by the Bioconductor R package Glimma v2.2.0 (*74*). *Z*-score transformed $\log_2$CPM values were used by the CRAN R package pheatmap v1.0.12 to produce the heatmaps. The GO term analysis was performed with topGO v2.44.0.

ULA assay

MDA-MB-231 cells transiently transfected with plasmids encoding GFP ($Mock^T$) or HSF2 ($HSF2oe^T$) were collected in assay medium 24 hours posttransfection. After counting, 2.7×10^3 cells were placed in each well of a 96-well ULA plate (#7007, Corning). The total volume in each well was 200 µl. Cells were imaged with a Zeiss Axio Vert.A1 microscope after 24 hours and using a 5x objective, numerical aperture (NA) 0.4. All images were analyzed with ImageJ software (version: 1.53f51) using the BioVoxxel Toolbox plugin (*75*). Briefly, the images were converted from 16 to 8 bit, and a Gaussian blur filter with a sigma (radius) of 13.00 was applied to reduce background. The perimeter of the spheroids was segmented with the thresholding algorithm of ImageJ choosing the black background option, and the extended particle analyzer option of the BioVoxxel Toolbox plugin was run with default settings.

Wound healing assay

MDA-MB-231 cells transiently transfected with plasmids encoding GFP ($Mock^T$) or HSF2 ($HSF2oe^T$) were collected in DMEM after a 24-hour recovery, and 0.5×10^6 cells were placed in a 12-well plate. After 21 hours, a pretreatment was started by switching to assay medium supplemented with TGF-β (10 ng/ml) or normal assay medium for the control cells. Following the 3-hour pretreatment, a scratch was made into the confluent cell sheet by using a 10-µl pipette tip. The rate of wound closure was followed by live-cell imaging with a frame interval of 5 min for 24 hours using Cell-IQ (Chip-Man Technologies). All images were analyzed with the ImageJ software (version: 1.53f51) using the magnetic resonance imaging (MRI) wound healing tool from https://github.com/MontpellierRessourcesImagerie/imagej_macros_and_scripts with the following settings: method = variance, variance filter radius = 10, threshold = 50, radius open = 4 min, and size = 10,000. The GitHub link was only used as an additional resource, as the source for the "MRI wound healing tool" ImageJ macro. After running the MRI wound healing tool, we filtered the results to keep the biggest area of each image in the time frame. The wound closure percentage compared to the initial wound area (0-hour measurement = 0%) was calculated for all time points. Last, to correct differences in the time of image acquisition and reduce the segmentation-associated variability, we interpolated the values of wound area with a second-degree polynomial equation.

Cell Counting Kit-8

The proliferation capacity of $Mock^S$ and $HSF2oe^S$ cells was assessed using CCK-8 according to the manufacturer's instructions (Dojindo, CK04). In brief, cells were seeded at a density of 2×10^3 cells per well in a 96-well plate and let to attach for 24 hours before treating with assay medium supplemented with TGF-β (10 ng/ml) for 24 and 72 hours. For the longer treatment, the fresh medium was changed after 48 hours. Following treatments, 10 µl of CCK-8 solution was added to each well of the plate and incubated for 2 hours. The absorbance was measured at 450 nm with a Hidex Sense Microplate Reader (Type 425-301, Hidex).

In vitro vasculogenic mimicry assay

Analysis of in vitro vasculogenic mimicry assay was used to examine the ability of $Mock^S$ and $HSF2oe^S$ to form cellular networks in three dimensions. The cells were pretreated with TGF-β for 24 hours. The wells of a 96-well plate were coated with 50 µl of Corning Matrigel LDEV-Free Growth Factor Reduced Basement Membrane Matrix (7 mg/ml; REF 354230, lot 0266001, Corning) and incubated for 30 min at 37°C to solidify the coating. Next, cells were counted, centrifuged, and resuspended in assay medium only (Ctrl) or in assay medium supplemented with TGF-β (10 ng/µl). A cell suspension of 100 µl containing 4×10^4 cells was added to each Matrigel-coated well. The plate was incubated at 37°C with 5% CO_2, and each well was imaged after 0 and 6 hours with a Zeiss Axio Vert.A1 microscope (NA 0.4) using a 5x objective. The formation of capillary-like structures was analyzed and quantified from the 6-hour images with the ImageJ Software (version: 1.53f51) using the Angiogenesis Analyzer toolset (invert filter, HUVEC Phase Contrast analysis) (*76*).

Organotypic 3D cultures

Organotypic 3D cultures were performed using µ-Slide 15 Well 3D plates (#81506, Ibidi). In brief, 10 µl of Matrigel (7 mg/ml) was added to the bottom of each well and incubated at 37°C for 1 hour. After incubation, 1×10^3 GFP^S or $HSF2^S$ cells were seeded in the wells in a total medium volume of 20 µl. The slide was then incubated at 37°C for 60 min to allow cell attachment to substrate. Next, the medium was aspirated and 20 µl of Matrigel (7 mg/ml) was added on top of the cells. After a 30-min incubation, 30 µl of medium or medium supplemented with TGF-β (10 ng/ml) was added to each well. The medium was changed every 2 days, and organotypic tumoroid

formation was followed by imaging the wells at days 4, 8, 12, and 16 with a Zeiss Axio Vert.A1 microscope using a 20x objective, NA 0.4.

Zebrafish xenografts

Experiments were performed as previously described in (*59*) under the license ESAVI/31414/2020 (granted by the Project Authorization Board of the Regional State Administrative Agency for Southern Finland) according to the regulations of the Finnish Act on Animal Experimentation (62/2006). Casper zebrafish strain (*77*) adults were placed in mating tanks and let to spawn overnight. The following day, embryos were collected and cultured in E3 medium (5 mM NaCl, 0.17 mM KCl, 0.33 mM $CaCl_2$ and 0.33 mM $MgSO_4$) supplemented with 0.2 mM phenylthiourea (PTU; Sigma-Aldrich) at 28.5°C. Pronase E was added to culture dishes after 24 hours to aid hatching. After 48 hours of cultivation, embryos were anesthetized with MS-222 (200 mg/liter; Sigma-Aldrich) and placed on agarose for cell transplantation. GFP^S and $HSF2oe^S$ HS578T cells were trypsinized, washed twice with PBS, and resuspended in PBS at a concentration of 1×10^6/10 μl. For immunofluorescence labeling, cells were detached in 5 ml of trypsin supplemented with 5 μM CellTracker Green CMFDA (Thermo Fisher Scientific), incubated for at least 5 min, washed twice with PBS, and resuspended at a concentration of 1×10^6/10 μl. Nanoinjection into the pericardial cavity of embryos was performed using the Nanoject II (Drummond Scientific) and in-house–produced capillary glass needles. For each nanoinjection, 4.6 nl of cell suspension was used. Following transplantation, embryos were removed from agarose, placed back on culture dishes, and cultured in E3-PTU at 33°C overnight.

At 1 dpi, successfully microinjected embryos were selected for experiments, anesthetized as previously described, and moved into a 96-well plate (one embryo per well). Embryos were imaged using a Nikon Eclipse Ti2 microscope equipped with a Plan UW 2x objective. Imaging was repeated at 4 dpi. The GFP intensity of the tumor was measured with FIJI software after background subtraction (rolling ball radius = 25, ImageJ version 1.49k) (*78*) with manual correction. The relative growth of the primary tumor was calculated by dividing the GFP intensity at 4 dpi with the GFP intensity at 1 dpi. Invading cells in the lens of embryos were not counted due to frequent autofluorescence. The number of invaded cells was counted manually at 1 and 4 dpi, and the fold change was calculated by dividing the obtained value at 4 dpi with that of 1 dpi. Data were analyzed in GraphPad Prism 8.3.0 using the unpaired two-tailed *t* test for statistical analyses, and results were plotted as means ± SD. For $Mock^S$ 16 and for $HSF2oe^S$ 19, zebrafish xenografts were analyzed. Malformed, dead, poorly oriented embryos, wells with two embryos, and wells where no GFP signal was detected were excluded from the analysis. Samples were not blinded for imaging or subsequent analyses.

For immunofluorescence labeling, zebrafish xenografts were fixed 24 hours postinjection in 4% PFA–PBS–0.2% Tween 20 for 2 hours at RT. After fixation, animals were washed 4 x 5 min in PBS–0.2% Tween 20, permeabilized in PBS–2% Triton X-100 for 3 hours at RT, and blocked in PBS–0.2% Triton X-100–5% FBS on rotation at 4°C overnight. The following day, primary antibody anti-Ki67 (8D5, Cell Signaling Technologies) was diluted in blocking solution (1:800) and the zebrafish were incubated in the primary antibody solution on rotation at 4°C overnight. The animals were then washed 6 x 30 min in PBS–0.2% Tween 20 at RT, after which the secondary antibody solution containing 1:400 Alexa Fluor 633 goat anti-mouse (A21052, Invitrogen) and 300 nM DAPI in blocking solution was added and incubated similarly as the primary antibody. The next day, animals were washed in PBS–0.2% Tween 20 6 x 30 min at RT and mounted on glass-bottom dishes using low-melting point agarose. Fixed and immunolabeled zebrafish embryos were imaged using a 3i CWU Spinning Disk confocal microscope with a 20x objective (Intelligent Imaging Innovations). Acquired images were analyzed with FIJI software. The area of GFP and Ki67 signals was segmented by manual thresholding. The relative area of Ki67 in the tumors was then calculated by dividing the measured area of Ki67 with the area of GFP. Data were analyzed in GraphPad Prism 8.3.0 using the unpaired two-tailed *t* test for statistical analyses and results were plotted as means ± SEM. For $Mock^S$ 12 and for $HSF2oe^S$ 11, zebrafish xenografts were analyzed. Samples were not blinded for imaging or subsequent analyses.

Mouse xenografts

Six- to 7-week-old virgin female NOD.CB17-Prkdcscid/NCrHsd mice (Envigo) were used in the tumor xenograft model. Mice were housed under standard conditions (12-hour/12-hour light/dark cycle) with food and water available ad libitum and randomly assigned to experimental groups. The National Animal Experiment Board authorized all animal studies and per The Finnish Act on Animal Experimentation (animal license number ESAVI-9339-04.10.07-2016).

Xenografts were generated as described in (*5*). Briefly, 1×10^5 DCIS.com lifeact-RFP cells were resuspended in 100 μl of a mixture of 50% Matrigel (diluted in PBS) before subcutaneous injection in the back of the mice. Tumor growth was measured with a caliper one to two times per week, and mice were euthanized 10 or 25 days postinoculation as indicated. Tumors were dissected, formalin fixed, and paraffin embedded. FFPE mouse xenograft tissues were sectioned and hematoxylin and eosin (H&E) labeled with standard procedures. Immunohistochemistry of FFPE sections was performed on deparaffinized sections after heat-mediated antigen retrieval in citrate buffer (10 mM trisodium citrate and 0.05% Tween 20 in ddH_2O). Tissue sections were blocked with 10% FBS-PBS blocking buffer for 1 hour at RT. Primary antibodies were diluted in the blocking buffer and incubated overnight at 4°C overnight in a humidified chamber [anti-keratin 8 1:1000 (Hybridoma Bank, TROMA-1); anti-HSF2 1:50 (HPA031455, Sigma-Aldrich); anti-Ki67 1:1000 (8D5, Cell Signaling Technology)]. After 3 x 5-min washes with PBS, the sections were incubated with the secondary antibodies diluted in blocking buffer for 1 hour at RT in a humidified chamber [anti-rabbit 488 secondary antibody (H+L) 1:400 (A21206 Thermo Scientific, Alexa Fluor 488); anti-rat 568 secondary antibody (H+L) 1:400 (A11077 Thermo Fisher Scientific, Alexa Fluor 568); anti-mouse 647 secondary antibody (H+L) 1:400 (A31571 Thermo Fisher Scientific, Alexa Fluor 647)]. Last, the sections were washed 3 x 5 min with PBS, 1:1000 DAPI (D1306 Life Technologies) in the second wash, and then 5 min with Milli-Q H_2O. Last, the sections were mounted under a #1.5 glass coverslip with MOWIOL (475904 Calbiochem) supplemented with 2.5% 1,4-diazabicyclo[2.2.2]octane (DABCO; D27802, Sigma-Aldrich).

Samples were imaged with the 3i Marianas CSU-W1 spinning disk (50-μm pinholes) confocal microscope using SlideBook 6 software. The objective used was a 40x Zeiss C-Apochromat water-immersion objective (NA 1.2). 3D images were acquired by taking *Z*-stacks with a 1-μm step size using the Photometrics Prime BSI scientific complementary metal-oxide-semiconductor (sCMOS) camera with a pixel size of 6.5 μm. Image analysis was conducted with ImageJ (version

1.52p). Images of tissue sections were projected as MIPs. The relative intensity of HSF2 was measured in the area of interest by segmenting the relevant area (keratin 8 for the epithelium and DAPI for nuclei). For proliferation analysis, the Ki67 signal was segmented and the epithelial nuclear signal was overlaid on epithelial nuclei to distinguish the fraction of proliferative nuclei. Similarly, the nuclear HSF2 signal was segmented and added on the nuclear Ki67 mask to create a double positive mask. This was then overlaid on Ki67-positive nuclei to distinguish the fraction of HSF2-positive area in proliferative nuclei.

Human tissue samples

Human breast tissue samples were obtained from patients undergoing breast surgery at the Department of Plastic and General Surgery at Turku University Hospital (Turku, Finland). All tissues were voluntarily donated upon written informed consent (ethical approval ETKM 23/2018; amendments 20.3.2018, 19.2.2019, and 17.1.2023) (table S3). Healthy breast tissue was obtained from three female patients undergoing breast reduction mammoplasty surgery. Breast tumor tissue was collected from patients undergoing mastectomy due to preinvasive (four samples) or invasive (three samples) breast carcinoma and were taken by a pathologist after diagnostic sample preparation. All tissues were surgically dissected and processed for fixation. Fixed frozen tissue sections were prepared from donor tissue as previously described (*79*). For immunofluorescence labeling, the frozen sections were first thawed for ~30 min at RT and then blocked and permeabilized in permeabilization buffer (2% BSA and 0.1% Triton X-100 in PBS) for 30 min at RT. Primary antibodies were incubated in 2% BSA in PBS overnight at 4°C [anti-keratin 8 1:1000 (Hybridoma Bank, TROMA-1); anti-HSF2 1:50 (HPA031455, Sigma-Aldrich); anti-HSF1 1:500 (PA3-017, Invitrogen); anti-Ki67 1:800 (clone 8D5, Cell Signaling Technology)]. After 3 x 10-min washes with PBS, the sections were incubated with the secondary antibodies diluted in 2% BSA-PBS for 1 hour at RT [anti-rat 488 secondary antibody (H+L) 1:400 (A21208 Thermo Fisher Scientific, Alexa Fluor 488); anti-rabbit 568 secondary antibody (H+L) 1:400 (A10042 Thermo Fisher Scientific, Alexa Fluor 568); anti-mouse 647 secondary antibody (H+L) 1:400 (A31571 Thermo Fisher Scientific, Alexa Fluor 647)]. Last, the sections were washed 3 x 10 min with PBS, 1:1000 DAPI (D1306, Life Technologies) in the second wash, and then 5 min with Milli-Q H_2O. Last, the sections were mounted under a #1.5 glass coverslip with MOWIOL (475904, Calbiochem) supplemented with 2.5% DABCO (D27802, Sigma-Aldrich).

Samples were imaged with the 3i Marianas CSU-W1 spinning disk (50-µm pinholes) confocal microscope using SlideBook 6 software. The objective used was a 20x Zeiss Plan-Apochromat objective (NA 0.8). The signal was detected with the following solid-state lasers and emission filters: 405-nm laser, 445/45 nm; 488-nm laser, 525/30 nm; 561-nm laser, 617/73 nm; and 640-nm laser, 692/40 nm. 3D images were acquired by taking *Z*-stacks with a 1-µm step size using the Photometrics Prime BSI sCMOS camera with a pixel size of 6.5 µm. Images were 16 bit with pixel dimensions of 2048 by 2048.

Image analysis was conducted with ImageJ (version 1.52p). Images of tissue sections were projected as MIPs. The relative intensity of HSF1 and HSF2 was measured in the area of interest by segmenting the relevant area (keratin 8 for the epithelium and DAPI for nuclei) and normalized by subtracting the background intensity. For proliferation analysis, the Ki67 signal was segmented and overlaid on epithelial nuclei to distinguish the fraction of proliferative nuclei. Similarly, the nuclear HSF1 or HSF2 signal was segmented and added on the nuclear Ki67 mask to create a double positive mask. This was then overlaid on Ki67-positive nuclei to distinguish the fraction of HSF1-positive or HSF2-positive proliferative nuclei.

Statistical analysis

For ULA assay, CCK-8, in vitro vasculogenic mimicry assay, immunofluorescence analysis of zebrafish xenografts, and supplementary RNA-seq data, the statistical significance was analyzed using paired two-tailed Student's *t* test and the data were plotted as means ± SEM. For the prolonged (1 dpi versus 4 dpi) xenograft assay, immunoblotting, immunofluorescence of cultured cells, and wound healing assay, the statistical significance was tested using an unpaired two-tailed *t* test and the data were plotted as means ± SD. For mouse xenograft and human tissue samples, data were analyzed in GraphPad Prism 10.1.2 using the Mann-Whitney test for statistical analyses, and results were plotted as violin plots showing the range of data points and the median value (line).

Visualization of data

Data were visualized using GraphPad Prism 8.3.0 and 10.4.1 Software (GraphPad Software).

Venn diagrams were generated with the BioVenn web application (https://biovenn.nl/) (*80*).

The GitHub link was only used as an additional resource, as the source for the "MRI wound healing tool" ImageJ macro.

Supplementary Materials

The PDF file includes:
Figs. S1 to S7
Tables S1 and S2
Legend for data S1

Other Supplementary Material for this manuscript includes the following:
Data S1

REFERENCES AND NOTES

1. G. M. Wilson, P. Dinh, N. Pathmanathan, J. D. Graham, Ductal carcinoma in situ: Molecular changes accompanying disease progression. *J. Mammary Gland Biol. Neoplasia* **27**, 101–131 (2022).
2. J. Wang, B. Li, M. Luo, J. Huang, K. Zhang, S. Zheng, S. Zhang, J. Zhou, Progression from ductal carcinoma in situ to invasive breast cancer: Molecular features and clinical significance. *Signal Transduct. Target. Ther.* **9**, 83 (2024).
3. P.-K. Lo, Y. Zhang, Y. Yao, B. Wolfson, J. Yu, S.-Y. Han, N. Duru, Q. Zhou, Tumor-associated myoepithelial cells promote the invasive progression of ductal carcinoma in situ through activation of TGFβ signaling. *J. Biol. Chem.* **292**, 11466–11484 (2017).
4. A. Dongre, R.-A. Weinberg, New insights into the mechanisms of epithelial-mesenchymal transition and implications for cancer. *Nat. Rev. Mol. Cell Biol.* **20**, 69–84 (2019).
5. E. Peuhu, G. Jacquemet, C. L. G. J. Scheele, A. Isomursu, M.-C. Laisne, L. M. Koskinen, I. Paatero, K. Thol, M. Georgiadou, C. Guzmán, S. Koskinen, A. Laiho, L. L. Elo, P. Boström, P. Hartiala, J. van Rheenen, J. Ivaska, MYO10-filopodia support basement membranes at pre-invasive tumor boundaries. *Dev. Cell* **57**, 2350–2364.e7 (2022).
6. J. H. Lee, J. Massagué, TGF-β in developmental and fibrogenic EMTs. *Semin. Cancer Biol.* **86**, 136–145 (2022).
7. R. Derynck, S. J. Turley, R. J. Akhurst, TGFβ biology in cancer progression and immunotherapy. *Nat. Rev. Clin. Oncol.* **18**, 9–34 (2021).
8. D. R. Principe, J. A. Doll, J. Bauer, B. Jung, H. G. Munshi, L. Bartholin, B. Pasche, C. Lee, P. J. Grippo, TGF-β: Duality of function between tumor prevention and carcinogenesis. *J. Natl. Cancer Inst.* **106**, djt369 (2014).
9. Y. Chen, C. Di, X. Zhang, J. Wang, F. Wang, J.-F. Yan, C. Xu, J. Zhang, Q. Zhang, H. Li, H. Yang, H. Zhang, Transforming growth factor β signaling pathway: A promising therapeutic target for cancer. *J. Cell. Physiol.* **235**, 1903–1914 (2020).
10. R. Gomez-Pastor, E. T. Burchfiel, D. J. Thiele, Regulation of heat shock transcription factors and their roles in physiology and disease. *Nat. Rev. Mol. Cell Biol.* **19**, 4–19 (2018).

11. M. J. Alasady, M. L. Mendillo, The heat shock factor code: Specifying a diversity of transcriptional regulatory programs broadly promoting stress resilience. *Cell Stress Chaperones* **29**, 735–749 (2024).
12. J. C. Pessa, J. Joutsen, L. Sistonen, Transcriptional reprogramming at the intersection of the heat shock response and proteostasis. *Mol. Cell* **84**, 80–93 (2024).
13. S. W. Kmiecik, M. P. Mayer, Molecular mechanisms of heat shock factor 1 regulation. *Trends Biochem. Sci.* **47**, 218–234 (2022).
14. M. C. Puustinen, L. Sistonen, Molecular mechanisms of heat shock factors in cancer. *Cells* **9**, 1202 (2020).
15. A. J. Sala, R. I. Morimoto, Protecting the future: Balancing proteostasis for reproduction. *Trends Cell Biol.* **32**, 202–215 (2022).
16. H. S. E. Hästbacka, A. J. Da Silva, L. Sistonen, E. Henriksson, A guide to heat shock factors as multifunctional transcriptional regulators. *FEBS J.*, 10.1111/febs.70139 (2025).
17. M. L. Mendillo, S. Santagata, M. Koeva, G. W. Bell, R. Hu, R. M. Tamimi, E. Fraenkel, T. A. Ince, L. Whitesell, S. Lindquist, HSF1 drives a transcriptional program distinct from heat shock to support highly malignant human cancers. *Cell* **150**, 549–562 (2012).
18. R. Scherz-Shouval, S. Santagata, M. L. Mendillo, L. M. Sholl, I. Ben-Aharon, A. H. Beck, D. Dias-Santagata, M. Koeva, S. M. Stemmer, L. Whitesell, S. Lindquist, The reprogramming of tumor stroma by HSF1 is a potent enabler of malignancy. *Cell* **158**, 564–578 (2014).
19. R. S. Smith, S. R. Takagishi, D. R. Amici, K. Metz, S. Gayatri, M. J. Alasady, Y. Wu, S. Brockway, S. L. Taiberg, N. Khalatyan, M. Taipale, S. Santagata, L. Whitesell, S. Lindquist, J. N. Savas, M. L. Mendillo, HSF2 cooperates with HSF1 to drive a transcriptional program critical for the malignant state. *Sci. Adv.* **8**, eabj6526 (2022).
20. C. Jacobs, S. Shah, W. C. Lu, H. Ray, J. Wang, N. Hockaden, G. Sandusky, K. P. Nephew, X. Lu, S. Cao, R. L. Carpenter, HSF1 inhibits antitumor immune activity in breast cancer by suppressing CCL5 to block $CD8^+$ T-cell recruitment. *Cancer Res.* **84**, 276–290 (2024).
21. Y. H. Zhao, M. Zhou, H. Liu, Y. Ding, H. T. Khong, D. Yu, O. Fodstad, M. Tan, Upregulation of lactate dehydrogenase A by ErbB2 through heat shock factor 1 promotes breast cancer cell glycolysis and growth. *Oncogene* **28**, 3689–3701 (2009).
22. S. Santagata, M. L. Mendillo, Y.-c. Tang, A. Subramanian, C. C. Perley, S. P. Roche, B. Wong, R. Narayan, H. Kwon, M. Koeva, A. Amon, T. R. Golub, J. A. Porco Jr., L. Whitesell, S. Lindquist, Tight coordination of protein translation and HSF1 activation supports the anabolic malignant state. *Science* **341**, 1238303 (2013).
23. R. L. Carpenter, S. Sirkisoon, D. Zhu, T. Rimkus, A. Harrison, A. Anderson, I. Paw, S. Qasem, F. Xing, Y. Liu, M. Chan, L. Metheny-Barlow, B. C. Pasche, W. Debinski, K. Watabe, H.-W. Lo, Combined inhibition of AKT and HSF1 suppresses breast cancer stem cells and tumor growth. *Oncotarget* **8**, 73947–73963 (2017).
24. S. Santagata, R. Hu, N. U. Lin, M. L. Mendillo, L. C. Collins, S. E. Hankinson, S. J. Schnitt, L. Whitesell, R. M. Tamimi, S. Lindquist, T. A. Ince, High levels of nuclear heat-shock factor 1 (HSF1) are associated with poor prognosis in breast cancer. *Proc. Natl. Acad. Sci. U.S.A.* **108**, 18378–18383 (2011).
25. J. K. Björk, M. Åkerfelt, J. Joutsen, M. C. Puustinen, F. Cheng, L. Sistonen, M. Nees, Heat-shock factor 2 is a suppressor of prostate cancer invasion. *Oncogene* **35**, 1770–1784 (2016).
26. F. Chen, Y. Fan, X. Liu, J. Zhang, Y. Shang, B. Zhang, B. Liu, J. Hou, P. Cao, K. Tan, Pan-cancer integrated analysis of HSF2 expression, prognostic value and potential implications for cancer immunity. *Front. Mol. Biosci.* **8**, 789703 (2022).
27. J. Joutsen, J. C. Pessa, O. Jokelainen, R. Sironen, J. M. Hartikainen, L. Sistonen, Comprehensive analysis of human tissues reveals unique expression and localization patterns of HSF1 and HSF2. *Cell Stress Chaperones* **29**, 235–271 (2024).
28. V. Mezger, M. Rallu, R. I. Morimoto, M. Morange, J. P. Renard, Heat shock factor 2-like activity in mouse blastocysts. *Dev. Biol.* **166**, 819–822 (1994).
29. M. Rallu, M. Loones, Y. Lallemand, R. Morimoto, M. Morange, V. Mezger, Function and regulation of heat shock factor 2 during mouse embryogenesis. *Proc. Natl. Acad. Sci. U.S.A.* **94**, 2392–2397 (1997).
30. F. R. Miller, S. J. Santner, L. Tait, P. J. Dawson, MCF10DCIS.com xenograft model of human comedo ductal carcinoma in situ. *J. Natl. Cancer Inst.* **92**, 1185–1186 (2000).
31. E. Frittoli, A. Palamidessi, P. Marighetti, S. Confalonieri, F. Bianchi, C. Malinverno, G. Mazzarol, G. Viale, I. Martin-Padura, M. Garré, D. Parazzoli, V. Mattei, S. Cortellino, G. Bertalot, P. P. Di Fiore, G. Scita, A RAB5/RAB4 recycling circuitry induces a proteolytic invasive program and promotes tumor dissemination. *J. Cell Biol.* **206**, 307–328 (2014).
32. T. D. Russell, S. Jindal, S. Agunbiade, D. Gao, M. Troxell, V. F. Borges, P. Schedin, Myoepithelial cell differentiation markers in ductal carcinoma in situ progression. *Am. J. Pathol.* **185**, 3076–3089 (2015).
33. F. Behbod, A. M. Gomes, H. L. Machado, Modeling human ductal carcinoma in situ in the mouse. *J. Mammary Gland Biol. Neoplasia* **23**, 269–278 (2018).
34. X.-H. Feng, R. Derynck, Specificity and versatility in TGF-β signaling through Smads. *Annu. Rev. Cell Dev. Biol.* **21**, 659–693 (2005).
35. H. Peinado, M. Quintanilla, A. Cano, Transforming growth factor β-1 induces snail transcription factor in epithelial cell lines: Mechanisms for epithelial mesenchymal transitions. *J. Biol. Chem.* **278**, 21113–21123 (2003).
36. W. E. Kutz, L. W. Wang, H. L. Bader, A. K. Majors, K. Iwata, E. I. Traboulsi, L. Y. Sakai, D. R. Keene, S. S. Apte, ADAMTS10 protein interacts with fibrillin-1 and promotes its deposition in extracellular matrix of cultured fibroblasts. *J. Biol. Chem.* **286**, 17156–17167 (2011).
37. S. A. Cain, E. J. Mularczyk, M. Singh, T. Massam-Wu, C. M. Kielty, ADAMTS-10 and -6 differentially regulate cell-cell junctions and focal adhesions. *Sci. Rep.* **6**, 35956 (2016).
38. A. V. Shinde, C. Humeres, N. G. Frangogiannis, The role of α-smooth muscle actin in fibroblast-mediated matrix contraction and remodeling. *Biochim. Biophys. Acta Mol. Basis Dis.* **1863**, 298–309 (2017).
39. M. P. Massett, B. C. Bywaters, H. C. Gibbs, J. P. Trzeciakowski, S. Padgham, J. Chen, G. Rivera, A. T. Yeh, D. M. Milewicz, A. Trache, Loss of smooth muscle α-actin effects on mechanosensing and cell-matrix adhesions. *Exp. Biol. Med.* **245**, 374–384 (2020).
40. A. Gharibi, S. La Kim, J. Molnar, D. Brambilla, Y. Adamian, M. Hoover, J. Hong, J. Lin, L. Wolfenden, J. A. Kelber, ITGA1 is a pre-malignant biomarker that promotes therapy resistance and metastatic potential in pancreatic cancer. *Sci. Rep.* **7**, 10060 (2017).
41. S. Kang, J. Yoo, K. Myung, PCNA cycling dynamics during DNA replication and repair in mammals. *Trends Genet.* **40**, 526–539 (2024).
42. T. Petojevic, J. J. Pesavento, A. Costa, J. Liang, Z. Wang, J. M. Berger, M. R. Botchan, Cdc45 (cell division cycle protein 45) guards the gate of the eukaryote replisome helicase stabilizing leading strand engagement. *Proc. Natl. Acad. Sci. U.S.A.* **112**, E249–E258 (2015).
43. P. Mukherjee, S. L. Winter, M. G. Alexandrow, Cell cycle arrest by transforming growth factor β1 near G_1/S is mediated by acute abrogation of prereplication complex activation involving an Rb-MCM interaction. *Mol. Cell. Biol.* **30**, 845–856 (2010).
44. M. Lei, The MCM complex: Its role in DNA replication and implications for cancer therapy. *Curr. Cancer Drug Targets* **5**, 365–380 (2005).
45. H. Kuivaniemi, G. Tromp, Type III collagen (COL3A1): Gene and protein structure, tissue distribution, and associated diseases. *Gene* **707**, 151–171 (2019).
46. S. Quintero-Fabián, R. Arreola, E. Becerril-Villanueva, J. C. Torres-Romero, V. Arana-Argáez, J. Lara-Riegos, M. A. Ramírez-Camacho, M. E. Alvarez-Sánchez, Role of matrix metalloproteinases in angiogenesis and cancer. *Front. Oncol.* **9**, 1370 (2019).
47. Y.-L. Liu, C.-K. Chou, M. Kim, R. Vasisht, Y.-A. Kuo, P. Ang, C. Liu, E. P. Perillo, Y.-A. Chen, K. Blocher, H. Horng, Y.-I. Chen, D. T. Nguyen, T. E. Yankeelov, M.-C. Hung, A. K. Dunn, H.-C. Yeh, Assessing metastatic potential of breast cancer cells based on EGFR dynamics. *Sci. Rep.* **9**, 3395 (2019).
48. A. J. Da Silva, H. S. E. Hästbacka, J. C. Luoto, R. E. Gough, L. S. Coelho-Rato, L. M. Laitala, B. T. Goult, S. Y. Imanishi, L. Sistonen, E. Henriksson, Proteomic profiling identifies a direct interaction between heat shock transcription factor 2 and the focal adhesion adapter talin-1. *FEBS J.* **291**, 4830–4848 (2024).
49. J. Joutsen, A. J. Da Silva, J. C. Luoto, M. A. Budzynski, A. S. Nylund, A. de Thonel, J. P. Concordet, V. Mezger, D. Sabéran-Djoneidi, E. Henriksson, L. Sistonen, Heat shock factor 2 protects against proteotoxicity by maintaining cell-cell adhesion. *Cell Rep.* **30**, 583–597.e6 (2020).
50. A. de Thonel, J. K. Ahlskog, K. Daupin, V. Dubreuil, J. Berthelet, C. Chaput, G. Pires, C. Leonetti, R. Abane, L. C. Barris, I. Leray, A. L. Aalto, S. Naceri, M. Cordonnier, C. Benasolo, M. Sanial, A. Duchateau, A. Vihervaara, M. C. Puustinen, F. Miozzo, F. Fergelot, E. Lebigot, A. Verloes, P. Gressens, D. Lacombe, J. Gobbo, C. Garrido, S. D. Westerheide, L. David, M. Petitjean, O. Taboureau, F. Rodrigues-Lima, S. Passermard, D. Saberan-Djoneidi, L. Nguyen, M. Lancaster, L. Sistonen, V. Mezger, CBP-HSF2 structural and functional interplay in Rubinstein-Taybi neurodevelopmental disorder. *Nat. Commun.* **13**, 7002 (2022).
51. Y. Zhang, P. B. Alexander, X. F. Wang, TGF-β family signaling in the control of cell proliferation and survival. *Cold Spring Harb. Perspect. Biol.* **9**, a022145 (2017).
52. B. P. Duncker, I. N. Chesnokov, B. J. McConkey, The origin recognition complex protein family. *Genome Biol.* **10**, 214 (2009).
53. S. L. Forsburg, Eukaryotic MCM proteins: Beyond replication initiation. *Microbiol. Mol. Biol. Rev.* **68**, 109–131 (2004).
54. R. P. Fisher, Secrets of a double agent: CDK7 in cell-cycle control and transcription. *J. Cell Sci.* **118**, 5171–5180 (2005).
55. J. M. Enserink, R. D. Kolodner, An overview of Cdk1-controlled targets and processes. *Cell Div.* **5**, 11 (2010).
56. S. Sengupta, S. Jana, A. Bhattacharyya, TGF-β-Smad2 dependent activation of CDC 25A plays an important role in cell proliferation through NFAT activation in metastatic breast cancer cells. *Cell. Signal.* **26**, 240–252 (2014).
57. S. Vega, A. V. Morales, O. H. Ocaña, F. Valdés, I. Fabregat, M. A. Nieto, Snail blocks the cell cycle and confers resistance to cell death. *Genes Dev.* **18**, 1131–1143 (2004).
58. A. De Donatis, F. Ranaldi, P. Cirri, Reciprocal control of cell proliferation and migration. *Cell Commun. Signal.* **8**, 20 (2010).
59. P. Pekkonen, S. Alve, G. Balistreri, S. Gramolelli, O. Tatti-Bugaeva, I. Paatero, O. Niiranen, K. Tuohinto, N. Perälä, A. Taiwo, N. Zinovkina, P. Repo, K. Icay, J. Ivaska, P. Saharinen, S. Hautaniemi, K. Lehti, P. M. Ojala, Lymphatic endothelium stimulates melanoma metastasis and invasion via MMP14-dependent Notch3 and β1-integrin activation. *eLife* **7**, e32490 (2018).

60. M. Y. Asghar, T. Lassila, I. Paatero, V. D. Nguyen, P. Kronqvist, J. Zhang, A. Slita, C. Löf, Y. Zhou, J. Rosenholm, K. Törnquist, Stromal interaction molecule 1 (STIM1) knock down attenuates invasion and proliferation and enhances the expression of thyroid-specific proteins in human follicular thyroid cancer cells. *Cell. Mol. Life Sci.* **78**, 5827–5846 (2021).
61. L. Shaashua, A. Ben-Shmuel, M. Pevsner-Fischer, G. Friedman, O. Levi-Galibov, S. Nandakumar, D. Barki, R. Nevo, L. E. Brown, W. Zhang, Y. Stein, C. Lior, H. S. Kim, L. Bojmar, W. R. Jarnagin, N. Lecomte, S. Mayer, R. Stok, H. Bishara, R. Hamodi, E. Levy-Lahad, T. Golan, J. A. Porco Jr., C. A. Iacobuzio-Donahue, N. Schultz, D. A. Tuveson, D. Lyden, D. Kelsen, R. Scherz-Shouval, BRCA mutational status shapes the stromal microenvironment of pancreatic cancer linking clusterin expression in cancer associated fibroblasts with HSF1 signaling. *Nat. Commun.* **13**, 6513 (2022).
62. B. Dong, A. M. Jaeger, P. F. Hughes, D. R. Loiselle, J. S. Hauck, Y. Fu, T. A. Haystead, J. Huang, D. J. Thiele, Targeting therapy-resistant prostate cancer via a direct inhibitor of the human heat shock transcription factor 1. *Sci. Transl. Med.* **12**, eabb5647 (2020).
63. Q. Dong, Y. Xiu, Y. Wang, C. Hodgson, N. Borcherding, C. Jordan, J. Buchanan, E. Taylor, B. Wagner, M. Leidinger, C. Holman, D. J. Thiele, S. O'Brien, H. H. Xue, J. Zhao, Q. Li, H. Meyerson, B. F. Boyce, C. Zhao, HSF1 is a driver of leukemia stem cell self-renewal in acute myeloid leukemia. *Nat. Commun.* **13**, 6107 (2022).
64. A. E. Pasqua, S. Y. Sharp, N. E. A. Chessum, A. Hayes, L. Pellegrino, M. J. Tucker, A. Miah, B. Wilding, L. E. Evans, C. S. Rye, N. Y. Mok, M. Liu, A. T. Henley, S. Gowan, E. De Billy, R. Te Poele, M. Powers, S. A. Eccles, P. A. Clarke, F. I. Raynaud, P. Workman, K. Jones, M. D. Cheeseman, HSF1 pathway inhibitor clinical candidate (CCT361814/NXP800) developed from a phenotypic screen as a potential treatment for refractory ovarian cancer and other malignancies. *J. Med. Chem.* **66**, 5907–5936 (2023).
65. J. Linares, J. A. Marín-Jiménez, J. Badia-Ramentol, A. Calon, Determinants and functions of CAFs secretome during cancer progression and therapy. *Front. Cell Dev. Biol.* **8**, 621070 (2021).
66. L. R. Tait, R. J. Pauley, S. J. Santner, G. H. Heppner, H. H. Heng, J. W. Rak, F. R. Miller, Dynamic stromal-epithelial interactions during progression of MCF10DCIS.com xenografts. *Int. J. Cancer* **120**, 2127–2134 (2007).
67. I. G. Cannell, K. Sawicka, I. Pearsall, S. A. Wild, L. Deighton, S. M. Pearsall, G. Lerda, F. Joud, S. Khan, A. Bruna, K. L. Simpson, C. M. Mulvey, F. Nugent, F. Qosaj, D. Bressan, CRUK IMAXT Grand Challenge Team, C. Dive, C. Caldas, G. J. Hannon, FOXC2 promotes vasculogenic mimicry and resistance to anti-angiogenic therapy. *Cell Rep.* **42**, 112791 (2023).
68. D. Yao, C. Dai, S. Peng, Mechanism of the mesenchymal-epithelial transition and its relationship with metastatic tumor formation. *Mol. Cancer Res.* **9**, 1608–1620 (2011).
69. J. E. Davis, B. Nemesure, S. Mehmood, V. Nayi, S. Burke, S. R. Brzostek, M. Singh, Her2 and Ki67 biomarkers predict recurrence of ductal carcinoma in situ. *Appl. Immunohistochem. Mol. Morphol.* **24**, 20–25 (2016).
70. N. Poulakaki, G. M. Makris, A. M. Papanota, F. Marineli, A. Marinelis, M. J. Battista, D. Boehm, A. Psyrri, T. N. Sergentanis, Ki-67 expression as a factor predicting recurrence of ductal carcinoma in situ of the breast: A systematic review and meta-analysis. *Clin. Breast Cancer* **18**, 157–167.e6 (2018).
71. A. Dobin, C. A. Davis, F. Schlesinger, J. Drenkow, C. Zaleski, S. Jha, P. Batut, M. Chaisson, T. R. Gingeras, STAR: Ultrafast universal RNA-seq aligner. *Bioinformatics* **29**, 15–21 (2013).
72. Y. Liao, G. K. Smyth, W. Shi, featureCounts: An efficient general purpose program for assigning sequence reads to genomic features. *Bioinformatics* **30**, 923–930 (2014).
73. M. D. Robinson, D. J. McCarthy, G. K. Smyth, edgeR: A Bioconductor package for differential expression analysis of digital gene expression data. *Bioinformatics* **26**, 139–140 (2010).
74. S. Su, C. W. Law, C. Ah-Cann, M.-L. Asselin-Labat, M. E. Blewitt, M. E. Ritchie, Glimma: Interactive graphics for gene expression analysis. *Bioinformatics* **33**, 2050–2052 (2017).
75. J. Brocher, biovoxxel/BioVoxxel-Toolbox: BioVoxxel Toolbox v2.6.0, Zenodo (2023); https://doi.org/10.5281/zenodo.8214743.
76. G. Carpentier, S. Berndt, S. Ferratge, W. Rasband, M. Cuendet, G. Uzan, P. Albanese, Angiogenesis analyzer for ImageJ—A comparative morphometric analysis of "Endothelial Tube Formation Assay" and "Fibrin Bead Assay". *Sci. Rep.* **10**, 11568 (2020).
77. R. M. White, A. Sessa, C. Burke, T. Bowman, J. LeBlanc, C. Ceol, C. Bourque, M. Dovey, W. Goessling, C. E. Burns, L. I. Zon, Transparent adult zebrafish as a tool for in vivo transplantation analysis. *Cell Stem Cell* **2**, 183–189 (2008).
78. J. Schindelin, I. Arganda-Carreras, E. Frise, V. Kaynig, M. Longair, T. Pietzsch, S. Preibisch, C. Rueden, S. Saalfeld, B. Schmid, J.-Y. Tinevez, D. J. White, V. Hartenstein, K. Eliceiri, P. Tomancak, A. Cardona, Fiji: An open-source platform for biological-image analysis. *Nat. Methods* **9**, 676–682 (2012).
79. O. Paavolainen, M. Peurla, L. M. Koskinen, J. Pohjankukka, K. Saberi, E. Tammelin, S.-R. Sulander, M. Valkonen, L. Mourao, P. Boström, N. Brück, P. Ruusuvuori, C. L. G. J. Scheele, P. Hartiala, E. Peuhu, Volumetric analysis of the terminal ductal lobular unit architecture and cell phenotypes in the human breast. *Cell Rep.* **43**, 114837 (2024).
80. T. Hulsen, J. Vlieg, W. Alkema, BioVenn—A web application for the comparison and visualization of biological lists using area-proportional Venn diagrams. *BMC Genomics* **9**, 488 (2008).

Acknowledgments: We thank the patients that voluntarily donated their tissue to this study and the clinical staff of Turku University Hospital. We thank all members of the Sistonen Laboratory for valuable comments and critical review of the manuscript. We thank J. Ivaska for kindly providing the MCF10-DCIS.com xenograft samples and M. L. Mendillo for the MDA-MB-231 HSF1-KO cell line. M. Peurla is acknowledged for assistance with the image analysis. We thank I. Paatero, the head of Zebrafish Facility at Turku Bioscience Centre, for assistance with zebrafish xenograft experiments. The Finnish Functional Genomics Centre is acknowledged for library preparation and sequencing of RNA-seq samples. The Finnish Functional Genomics Centre is supported by the University of Turku, Åbo Akademi University, and Biocenter Finland. The tissue samples were prepared at Histocore (Institute of Biomedicine, University of Turku), and microscopy analyses were conducted at The Cell Imaging and Cytometry Core facility (Turku Bioscience, University of Turku and Åbo Akademi University, and Biocenter Finland). **Funding:** This work was supported by the Research Council of Finland (S.G., E.P., and L.S.); Sigrid Jusélius Foundation (E.P. and L.S.); Cancer Foundation Finland (E.P. and L.S.); Jane and Aatos Erkko Foundation (E.P. and L.S.); Åbo Akademi University funded Doctoral Position (J.C.P.); The Finnish Cultural Foundation, Kymenlaakso Regional Fund (J.C.P.); Turku Doctoral Program in Molecular Medicine (O.P.); Swedish Cultural Foundation (M.C.P.); K. Albin Johansson's Foundation (H.S.E.H., M.C.P., and A.J.D.S.); Magnus Ehrnrooth Foundation (A.J.D.S.); The Medical Research Foundation Liv och Hälsa (A.J.D.S. and L.S.); Finnish Cultural Foundation (A.J.D.S. and S.G.); The Finnish Cultural Foundation, Lapland Regional Fund (J.J.); Lapland Hospital District Research Grant (J.J.); and The Hospital District of Southwestern Finland (E.P.). **Author contributions:** Conceptualization: J.C.P., M.C.P., A.J.D.S., S.P., P.B., P.H., E.P., J.J., and L.S. Data curation: M.C.P., A.J.D.S., E.P., and L.S. Formal analysis: J.C.P., O.P., H.S.E.H., M.C.P., and A.J.D.S. Funding acquisition: J.C.P., O.P., M.C.P., E.P., J.J., and L.S. Investigation: J.C.P., O.P., M.C.P., S.P., and E.P. Methodology: J.C.P., M.C.P., A.J.D.S., S.G., and E.P. Project administration: J.C.P., M.C.P., E.P., and L.S. Resources: M.C.P., P.B., P.H., E.P., and L.S. Supervision: J.C.P., M.C.P., E.P., and L.S. Validation: J.C.P., O.P., M.C.P., and S.P. Visualization: J.C.P., O.P., H.S.E.H., M.C.P., E.P., J.J., and L.S. Writing—original draft: J.C.P., M.C.P., E.P., J.J., and L.S. Writing—review and editing: J.C.P., O.P., M.C.P., A.J.D.S., S.P., P.H., E.P., J.J., and L.S. **Competing interests:** The authors declare that they have no competing interests. **Data and materials availability:** All data needed to evaluate the conclusions in the paper are present in the paper and/or the Supplementary Materials. The original data are available at the Gene Expression Omnibus (GEO) database under accession number GSE211020.

Submitted 10 April 2025
Accepted 1 August 2025
Published 3 September 2025
10.1126/sciadv.ady1289